

Experimental and Theoretical Validation of High Efficiency and Robust Electrocatalytic Response of One-Dimensional (1D) (Mn,Ir)O₂:10F Nanorods for the Oxygen Evolution Reaction in PEM-Based Water Electrolysis

Shrinath Dattatray Ghadge,[†] Oleg I. Velikokhatnyi,^{‡,§} Moni K. Datta,^{‡,§} Pavithra M. Shanthi,[†] Susheng Tan,^{||} Krishnan Damodaran,[⊥] and Prashant N. Kumta^{*,†,‡,§,#,∇} 

[†]Chemical and Petroleum Engineering, Swanson School of Engineering, University of Pittsburgh, Pittsburgh, Pennsylvania 15261, United States

[‡]Department of Bioengineering, Swanson School of Engineering, University of Pittsburgh, Pittsburgh, Pennsylvania 15261, United States

[§]Center for Complex Engineered Multifunctional Materials, University of Pittsburgh, Pittsburgh, Pennsylvania 15261, United States

^{||}Department of Electrical and Computer Engineering and Petersen Institute of Nanoscience and Engineering, University of Pittsburgh, Pittsburgh, Pennsylvania 15260, United States

[⊥]Department of Chemistry, University of Pittsburgh, Pittsburgh, Pennsylvania 15260, United States

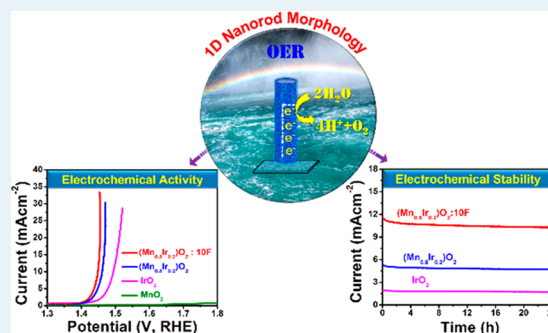
[#]Mechanical Engineering and Materials Science, University of Pittsburgh, Pittsburgh, Pennsylvania 15261, United States

[∇]School of Dental Medicine, University of Pittsburgh, Pittsburgh, Pennsylvania 15217, United States

Supporting Information

ABSTRACT: Development of highly efficient, earth-abundant, and cost-effective electrocatalysts for the kinetically sluggish and energy-intensive anodic oxygen evolution reaction (OER) is crucial for realizing the large-scale commercialization of proton exchange membrane based water electrolysis (PEMWE). Herein, we report the results of one-dimensional (1D) nanorods (NRs) containing an ultralow amount of noble metal (iridium, Ir) and 10 wt % fluorine (F) doped (Mn_{0.8}Ir_{0.2})O₂:10F as an efficient anode electrocatalyst, synthesized via a simple hydrothermal and wet chemical approach for the acidic OER. The as-synthesized (Mn_{0.8}Ir_{0.2})O₂:10F NRs demonstrate promising electrocatalytic performance for the OER with significantly lower overpotential (η) and higher current density than state of the art IrO₂ and many other electrocatalysts containing noble metal/reduced noble metal. Owing to the presence of 1D channels of the nanorod architecture and the unique electronic structure obtained upon formation of an F-containing solid solution, the (Mn_{0.8}Ir_{0.2})O₂:10F NRs exhibit low charge transfer resistance ($\sim 2.5 \Omega \text{ cm}^2$), low Tafel slope ($\sim 38 \text{ mV dec}^{-1}$), low water contact angle ($\sim 18^\circ$), high electrochemical active surface area (ECSA $\approx 704.76 \text{ m}^2 \text{ g}^{-1}$), high roughness factor (~ 2114), and notable OER performance with ~ 6 -, ~ 2.1 -, and ~ 2.2 -fold higher electrocatalytic activity in comparison to IrO₂, (Mn_{0.8}Ir_{0.2})O₂ NRs and a 2D thin film of (Mn_{0.8}Ir_{0.2})O₂:10F, respectively. The significantly higher ECSA and BET specific activity ($0.11 \text{ mA cm}^{-2}_{\text{BET}}$), mass activity (40 Ag^{-1}), and TOF (0.01 s^{-1}) at an overpotential (η) of 220 mV suggest the intrinsically higher catalytic activity of (Mn_{0.8}Ir_{0.2})O₂:10F NRs in comparison to other as-synthesized electrocatalysts. In addition, (Mn_{0.8}Ir_{0.2})O₂:10F NRs function as robust electrocatalysts by delivering a current density of 10 mA cm^{-2} at $\eta \approx 200 \text{ mV}$ and displaying long-term durability, devoid of any degradation of the catalytic activity, suggesting the structural robustness for displaying prolonged OER activity. Herein, on the basis of the synergistic effects of tailoring of 2D material length scales into a 1D nanorod framework and the corresponding formation of an F-substituted unique solid solution structure (as validated by density functional theory), (Mn_{0.8}Ir_{0.2})O₂:10F NRs offer promise for an efficient OER in PEMWE.

KEYWORDS: proton exchange membrane (PEM) based water electrolysis, acidic oxygen evolution reaction (OER), electrocatalyst, one-dimensional nanorods, density functional theory (DFT)



1. INTRODUCTION

The alarming concerns related to rapid depletion of conventional fossil fuels and the associated deleterious warning effects

Received: July 23, 2018

Revised: January 3, 2019

Published: January 16, 2019

of global warming have provided tremendous impetus to develop alternative clean, environmentally friendly, and sustainable energy sources which can alleviate the global reliance on rapidly depleting fossil fuels (natural gas, coal, oil).^{1–3} With these constant incessant concerns, hydrogen (H_2) gas having a completely noncarbonaceous nature, higher energy density (~ 120 MJ/kg) than petroleum-based energy sources (~ 45 MJ/kg) and environmental friendliness offers an ecologically ideal energy vector to counter the growing global energy demand. The burgeoning positive influence of hydrogen fuel has thus, garnered immense attention as the foremost energy carrier over the past decade.^{4–7} Along these lines, the generation of clean and sustainable hydrogen fuel via advantageous acidic electrolysis, i.e. proton exchange membrane (PEM) based water electrolysis, is hitherto considered as one of the most efficient and reliable technologies among all other conventional hydrogen production approaches.^{2,8} Although PEM water electrolysis is a promising approach for large-scale generation of ultrahigh-purity (UHP) hydrogen, commercial development of this technology has been largely constrained due to the energy-intensive, technologically challenging, and sluggish anodic oxygen evolution reaction (OER; $2H_2O \rightarrow O_2 + 4H^+ + 4e^-$), which requires an electrochemical overpotential of ~ 1.8 – 2 V, which is significantly higher than the standard thermodynamic water splitting OER value of ~ 1.23 V.^{8–10} To address this bottleneck, platinum group metal (PGM) based electrocatalysts such as Pt, RuO_2 , and IrO_2 are considered as pioneering electrocatalysts which facilitate the sustained oxygen evolution under highly acidic conditions and exhibit excellent electrocatalytic OER performance toward PEM-based water electrolysis.^{11,12} However, the very high cost (e.g., $\$210/g_{IrO_2}$) and environmental scarcity (~ 0.001 – 0.0003 ppm in earth's crust)¹³ of these benchmark precious metal electrocatalysts has seriously restricted their applications in a large-scale PEM water electrolyzer.^{8,14} Therefore, the identification, synthesis, and development of novel reduced noble metal containing electrocatalysts, unveiling remarkable electrocatalytic activity with low overpotential and excellent long-term electrochemical stability, superior to state of the art OER electrocatalysts (IrO_2) under the acidic operating conditions of the OER, will universally assist in the reduction of capital cost of PEM water electrolyzer cells.¹⁵ The consequent scientific advances will help trigger commercialization, enabling clean and regenerated energy production by making the water splitting reaction more energy efficient.^{2,16,17}

In view of the above considerations, to realize the much desired progress, our previous research efforts over the past decade in the PEM water electrolysis and OER electrode development arena have encompassed exploiting the unique strategies of solid solution formation utilizing ultralow noble metal (Ir/Ru) content with earth-abundant and low-cost catalyst supports (Sn, Nb, Mn) combined with anionic doping (F) to improve the IrO_2/RuO_2 electrode performance (activity as well as stability).^{2,16–21} In one of our previous reports,² utilizing this solid solution formation strategy, we have exploited the first-principles theoretical calculations of total energies and electronic structures and have accordingly established the major paradigm for enhancing the electrocatalytic activity of IrO_2 by generating a solid solution OER electrocatalyst of $(Mn_{1-x}Ir_x)O_2 \cdot 10F$ ($x = 0.2, 0.3, 0.4$). These novel compositions comprise earth-abundant manganese oxide (MnO_2) combined with the anionic dopant fluorine (F) serving as the primary electronic conductivity stimulant juxtaposed with an ultralow noble metal content of Ir. Arising from the unique electronic/molecular

structure and beneficial solid solution formation, the as-synthesized $(Mn_{1-x}Ir_x)O_2 \cdot 10F$ electrocatalyst system fabricated in the 2D thin film architecture demonstrated remarkable electrocatalytic performance with a significantly lower onset potential of ~ 1.35 V (vs RHE): i.e. ~ 80 mV lower than that of IrO_2 (~ 1.43 V) in acid-mediated water electrolysis.² In addition, the $(Mn_{1-x}Ir_x)O_2 \cdot 10F$ electrocatalyst with substantial reduction (~ 80 atom %) in the noble metal content ($(Mn_{0.8}Ir_{0.2})O_2 \cdot 10F$) exhibited excellent OER activity (~ 7 -fold higher than IrO_2 film) as well as excellent durability in comparison to IrO_2 film electrocatalyst.²

With this previous work serving as a guide and by exploiting the attributes of nanostructures engineering to further enhance the electrocatalytic performance of 2D thin film solid solution electrocatalysts, we have embarked on a pathway to design a highly active, highly robust, and scalable electrocatalysts system by tailoring the material length scales into one-dimensional (1D) nanoscale architectures. Among the various electrocatalyst development strategies, the design and fabrication of nanostructured one-dimensional (1D) electrocatalyst architectures such as nanowires (NWs), nanorods (NRs), nanotubes (NTs), etc. has been gathering significant attention^{22–26} and a plethora of research funding has been invested to fabricate various 1D electrocatalysts such as CoP NRs,²⁷ Ni_3S_2 NRs,²⁸ Pt NTs,²⁵ nitrogen-containing carbon nanotubes (NCNTs),^{29,30} TiO_2 NRs,^{31–33} Pt-Ni- TiO_2 NTs,^{34–36} Pt-Ru/Co NWs,^{35,36} Co_4N NWs,³⁷ Ir-Ni and Ir-Co NWs,³⁸ etc. with tunable morphology and phase resulting in distinct performances in electrolytic/ photoelectrochemical water splitting as well as in the direct methanol fuel cell (DMFC) research area.^{35,39}

It is well-known that, in general, 1D nanostructures offer various benefits either by favorably exposing the vicinal (i.e. high-index) facets (or active sites for reaction) and/or electrically linking these active sites for facile electron or charge transport within the 1D channels of nanomaterials.²⁴ In addition, the 1D materials possess high active specific surface areas, large aspect ratio (L/D), high active-site densities, and high roughness factors which can substantially increase the efficiency and performance of electrocatalyst materials.³⁵ Furthermore, due to the presence of 1D channels and lattice planes with fewer crystal boundaries, 1D nanomaterials encounter fast charge transport pathways with reduced scattering offering lower charge transfer resistance (R_{ct}) and high electronic conductivity.³⁵ In addition, it is reported that the presence of sufficient porosity and open space between the adjacent 1D channels is significantly beneficial for enabling rapid release of oxygen bubbles as well as offering excellent electrocatalyst to electrolyte contact due to the ease of accessibility of the electrolyte molecules into the deep portion of the electrode/catalyst surface.^{24,40} This evidently expedites the reaction kinetics, offering faster mass as well as charge transport. In addition to these various benefits to enhance the catalytic activity, 1D nanostructures are also well-known in terms of their excellent electrocatalytic stability.³⁵ On the basis of these previous studies, an asymmetric structure of 1D architecture is regarded as a beneficial factor for displaying superior catalytic stability while also alleviating the dissolution and suppression of the physical ripening processes which commonly occur in nanoparticulate or film-based catalyst materials.^{35,41–43}

Thus, as a culmination of all of these excellent attributes, 1D morphologies are primarily regarded as essential building blocks for the development of high-performance electrocatalysts. For

example, in our recently reported study, we have successfully demonstrated the suitability of 1D vertically aligned nanotubes (VANTs) containing an ultralow amount of noble metal and F substituted ($\text{Sn}_{0.8}\text{Ir}_{0.2}$) O_2 :10F as an efficient electrocatalyst system for the OER in the PEM-based water electrolysis system.³ The as-synthesized 1D NTs unveiled excellent electrochemical performance with significant ~ 2.3 -fold higher electrocatalytic activity, lower charge transfer resistance, and higher electrochemically active surface area (ECSA) in comparison to that of the 2D thin film architecture of identical composition of ($\text{Sn}_{0.8}\text{Ir}_{0.2}$) O_2 :10F.^{3,16} Thus, following in the same vein of electrocatalyst development displaying significant enhancement in the electrocatalytic performance of our previously reported ($\text{Mn}_{1-x}\text{Ir}_x$) O_2 :10F system,² herein, we report for the first time, the synthesis of 1D nanorods of ($\text{Mn}_{1-x}\text{Ir}_x$) O_2 :10F ($x = 0.2$) and also correspondingly demonstrate the system as a highly efficient and robust OER electrocatalyst morphology for PEM water electrolysis. The OER performance of the as-synthesized ($\text{Mn}_{0.8}\text{Ir}_{0.2}$) O_2 :10F NRs has been compared with the state of the art IrO_2 and our previously reported 2D thin film architecture of ($\text{Mn}_{0.8}\text{Ir}_{0.2}$) O_2 :10F.² In order to fabricate the 1D nanomaterials, various techniques such as physical vapor deposition,⁴⁴ thermal decomposition,⁴⁵ vapor–liquid–solid deposition,⁴⁶ etc. have been reported. Among the various techniques, a hydrothermal- or autoclave-based approach is comparatively simple, time efficient, inexpensive, and easily scalable for the reliable fabrication of various 1D architectures, offering facile control over the size and shape of the various nanostructured materials. Therefore, herein, 1D solid solution NRs of ($\text{Mn}_{0.8}\text{Ir}_{0.2}$) O_2 :10F have been synthesized using a two-step method. In the first step, MnO_2 NRs are synthesized via a simple and inexpensive hydrothermal approach. The second step involves the wet chemical approach of incorporating Ir and F into the MnO_2 framework, followed by calcination to form the solid solution of (Mn,Ir) O_2 :F.

In the current study, as anticipated, the as-synthesized pure 1D ($\text{Mn}_{0.8}\text{Ir}_{0.2}$) O_2 :10F NRs exhibited remarkable electrocatalytic performance for the OER in acidic media by attaining the benchmark current density of 10 mA cm^{-2} at a low overpotential (η) of 200 mV, superior to the state of the art IrO_2 , ($\text{Mn}_{0.8}\text{Ir}_{0.2}$) O_2 :10F 2D thin film, and many other reported electrocatalysts containing noble metal/reduced noble metal for the acidic OER, including an Ir-doped cryptomelane-type manganese oxide [$\text{K}_{1.65}(\text{Mn}_{0.78}\text{Ir}_{0.22})_8\text{O}_{16}$] based electrocatalyst system ($\eta \approx 340 \text{ mV}$) as recently reported by Sun et al.⁴⁷ Furthermore, ($\text{Mn}_{0.8}\text{Ir}_{0.2}$) O_2 :10F NRs demonstrated significantly lower charge transfer resistance ($2.5 \Omega \text{ cm}^2$), lower Tafel slope (38 mV dec^{-1}), and particularly, higher ECSA as well as BET specific activity combined with a high turnover frequency (TOF) of $\sim 0.01 \text{ s}^{-1}$ at $\eta = 220 \text{ mV}$. In addition, the OER stability test conducted using ($\text{Mn}_{0.8}\text{Ir}_{0.2}$) O_2 :10F NRs demonstrated no significant decay in the current density, suggesting its excellent structural and morphological robustness, as witnessed from the poststability characterization of the electrocatalytic activity. It is therefore worth mentioning that the superior electrocatalytic performance of the as-synthesized ($\text{Mn}_{0.8}\text{Ir}_{0.2}$) O_2 :10F NRs is well supported by our density functional theory (DFT) computational calculations, which further illustrate that F-substituted ($\text{Mn}_{0.8}\text{Ir}_{0.2}$) O_2 :10F NRs possess lower overpotential and superior catalytic activity contrasted with those of the corresponding 2D film, leading to the excellent electrocatalytic activity with significant reduction (~ 80 atom

%) in the noble metal content. Thus, all of these results taken in total, and discussed in detail in the following sections, indicate the promise of ($\text{Mn}_{0.8}\text{Ir}_{0.2}$) O_2 :10F NRs as an attractive OER electrocatalyst for efficient and sustainable hydrogen production using the PEM-based water splitting approach.

2. EXPERIMENTAL METHODOLOGY

2.1. Materials. Manganese(II) sulfate monohydrate ($\text{MnSO}_4 \cdot \text{H}_2\text{O}$, $\geq 99\%$, Sigma-Aldrich), potassium permanganate (KMnO_4 , $\geq 99.0\%$, Fisher Scientific), iridium tetrachloride (IrCl_4 , 99.5%, Alfa Aesar), and ammonium fluoride (NH_4F , 98%, Alfa Aesar) were used as precursors for electrocatalyst synthesis. Nafion 117 (5 wt % solution in lower aliphatic alcohols, Sigma-Aldrich) was used as a binder. Deionized (DI) water (18 M Ω cm, Milli-Q Academic, Millipore) was used throughout the experiments. All of the chemical reagents were used as received without any further purification.

2.2. Preparation of Electrocatalyst Materials.
2.2.1. Synthesis of MnO_2 Nanorods (NRs). A hydrothermal (autoclave) approach was utilized for the synthesis of MnO_2 NRs.⁴⁸ In a typical synthesis of MnO_2 NRs, $\text{MnSO}_4 \cdot \text{H}_2\text{O}$ (0.2 g) and KMnO_4 (0.5 g) were dissolved in 100 mL of DI water with continuous stirring for 30 min at room temperature to form a homogeneous solution. This solution was then transferred into a Teflon-lined stainless steel autoclave (120 mL capacity), and the autoclave was subjected to heat treatment at $160 \text{ }^\circ\text{C}$ for 12 h (ramp rate $10 \text{ }^\circ\text{C/min}$). After the reaction involving generation of the corresponding MnO_2 ($2\text{KMnO}_4 + 3\text{MnSO}_4 + 2\text{H}_2\text{O} \rightarrow 5\alpha\text{-MnO}_2 + \text{K}_2\text{SO}_4 + 2\text{H}_2\text{SO}_4$) was complete, the autoclave was naturally cooled to room temperature. The obtained brownish solid product was thoroughly washed with DI water several times (9500 rpm, 3 min), followed by drying overnight in air at $60 \text{ }^\circ\text{C}$ for further characterizations.

2.2.2. Synthesis of ($\text{Mn}_{0.8}\text{Ir}_{0.2}$) O_2 and ($\text{Mn}_{0.8}\text{Ir}_{0.2}$) O_2 :10F NRs. For the preparation of ($\text{Mn}_{0.8}\text{Ir}_{0.2}$) O_2 and 10 wt % F doped ($\text{Mn}_{0.8}\text{Ir}_{0.2}$) O_2 (($\text{Mn}_{0.8}\text{Ir}_{0.2}$) O_2 :10F), a stoichiometric amount of IrCl_4 was added to the DI water along with a stoichiometric amount of the as-prepared MnO_2 . Similarly, for the synthesis of ($\text{Mn}_{0.8}\text{Ir}_{0.2}$) O_2 :10F, stoichiometric amounts of IrCl_4 and NH_4F were mixed in the DI water along with the appropriate amount of the as-prepared MnO_2 . These solutions were stirred vigorously for 1 h and transferred into the alumina crucibles and then, dried in an electric oven at $60 \text{ }^\circ\text{C}$ for ~ 3 h. The crucibles containing the dried oxide precursors were then subjected to heat treatment in air at $400 \text{ }^\circ\text{C}$ (ramp rate $10 \text{ }^\circ\text{C/min}$) for 4 h in order to form the corresponding ($\text{Mn}_{0.8}\text{Ir}_{0.2}$) O_2 and ($\text{Mn}_{0.8}\text{Ir}_{0.2}$) O_2 :10F solid solution electrocatalysts, respectively. The obtained electrocatalyst products were washed with DI water several times and then dried overnight in air at $60 \text{ }^\circ\text{C}$ for further characterizations. In addition, in order to investigate the influence of F on the as-synthesized MnO_2 , the F-doped MnO_2 (MnO_2 :10F) has also been synthesized by employing the approach described above. Herein, it is worth mentioning that the major objective of the present study was to demonstrate the superior electrochemical performance of 1D ($\text{Mn}_{0.8}\text{Ir}_{0.2}$) O_2 NRs in comparison to that of our previously reported² 2D thin film of ($\text{Mn}_{0.8}\text{Ir}_{0.2}$) O_2 under identical synthesis (atomic ratio, calcination temperature and time, mass loading, etc.) as well as OER operating conditions. Therefore, in the current work, in order to execute an unbiased comparison between 1D NRs and 2D thin film, we have fabricated ($\text{Mn}_{0.8}\text{Ir}_{0.2}$) O_2 NRs at a calcination temperature of $400 \text{ }^\circ\text{C}$. Furthermore, it is well-known that $\alpha\text{-MnO}_2$ initiates its transformation from an $\alpha\text{-MnO}_2$ to an α

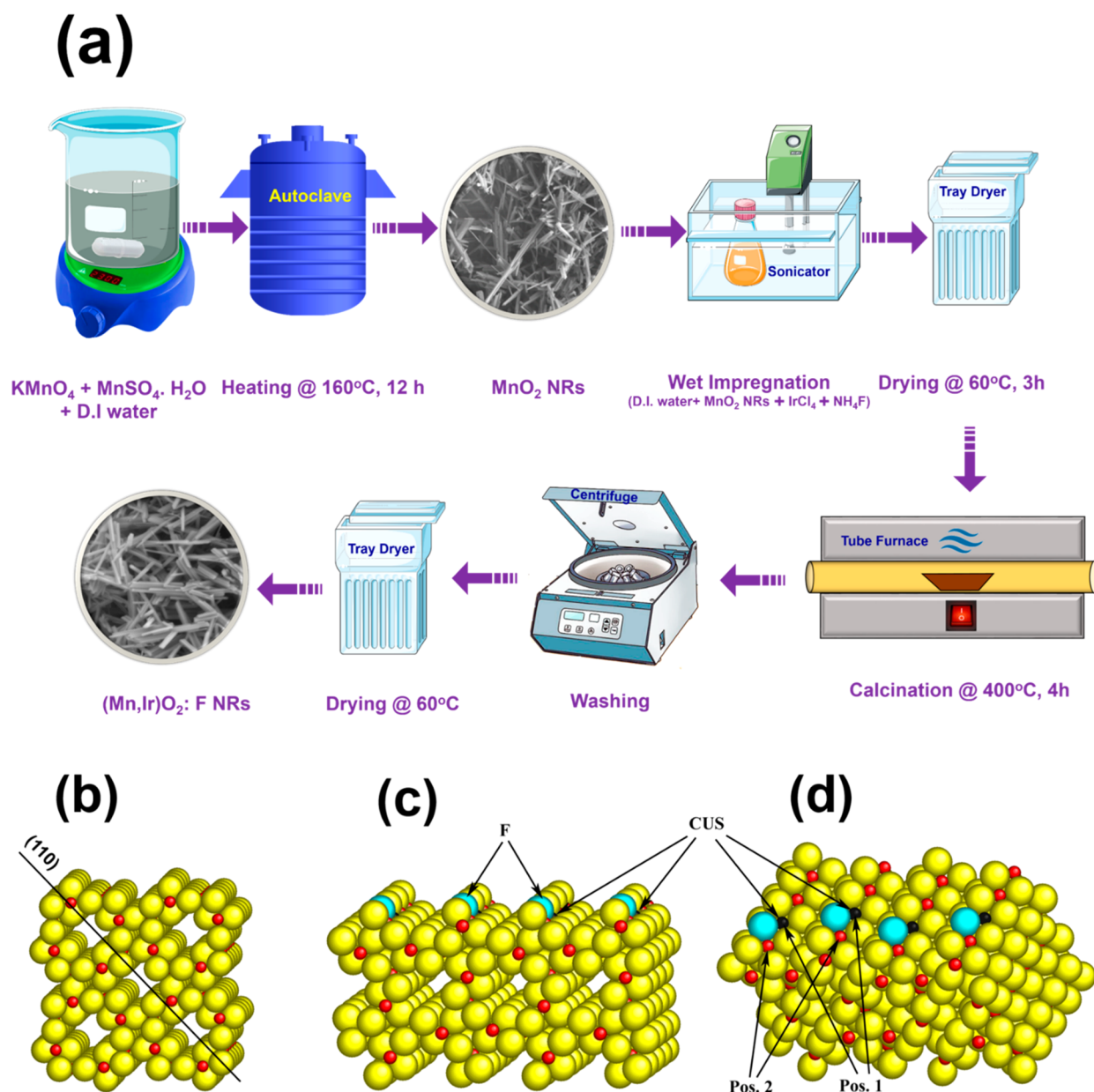


Figure 1. (a) Schematic illustration for the synthesis process of $(\text{Mn}_{0.8}\text{Ir}_{0.2})\text{O}_2:10\text{F NRs}$, (b) General view of $\alpha\text{-MnO}_2$ crystal structure with coordinatively unsaturated sites (CUS) at (110) crystallographic surfaces. (c, d) The (110) surface at different angles. Pos.1 and Pos.2 represent two possible positions of Ir atoms considered in the present study.

Mn_2O_3 phase beyond the calcination temperature of 500°C (typically $600\text{--}800^\circ\text{C}$).^{47,49} Thus, in order to prevent any undesired phase transformation during the calcination process, we have performed the electrocatalyst synthesis and calcination of $(\text{Mn,Ir})\text{O}_2$ at 400°C . It should be noted that a similar calcination temperature (400°C) has been utilized for the thin film fabrication of Ir-Mn oxide based electrocatalysts in the literature,⁵⁰ wherein the optimum electrocatalytic performance has been achieved at 400°C . The schematic illustration of the synthesis process for generating MnO_2 and $(\text{Mn}_{0.8}\text{Ir}_{0.2})\text{O}_2:10\text{F NRs}$ is depicted in Figure 1a.

2.2.3. Synthesis of IrO_2 Nanoparticles. For the synthesis of IrO_2 nanoparticles, a well-known modified Adams fusion method was utilized.¹⁸ Specifically, IrCl_4 and NaNO_3 were separately dissolved in DI water. The solution containing the dissolved IrCl_4 was then mixed with excess NaNO_3 solution.

Next, the resulting solution mixture was thoroughly stirred for ~ 2 h to make it completely homogeneous. The water from this uniform mixture was then evaporated using a heating furnace operated at 60°C , followed by heat treatment in air at 500°C for 1 h (ramp rate $10^\circ\text{C}/\text{min}$). The thermally treated solid mixture was naturally cooled to room temperature and then crushed into a fine powder using an agate mortar and pestle. This powder was then vigorously washed using DI water, and the resulting product (IrO_2) was then dried in an oven at 60°C for further characterizations. Herein, for the synthesis of IrO_2 , the calcination temperature of 500°C was selected on the basis of various critical viewpoints elucidated in the literature. For example, in the study conducted by Geiger et al.,⁵¹ it has been observed and reported that the catalytic activity (for the acidic OER) of IrO_2 starts declining from a calcination temperature of $400\text{--}600^\circ\text{C}$ and more stable electrodes are formed at $T \geq 400$

°C. In addition, on the basis of the intrinsic activity and dissolution of IrO₂-based electrocatalysts, Geiger et al.⁵¹ concluded that the IrO₂ electrodes synthesized at ~500 °C were identified as the most promising for the acidic OER. Added to this, Siracusano et al.⁵² reports that a mild annealing process (~500 °C) for IrO₂ is critical to avoid excessive growth of the catalyst particles while favoring the proper crystallization in the bulk. Thus, in agreement with these viewpoints, in order to attain optimum electrocatalytic performance (activity and stability) as well as to form crystalline IrO₂, we have employed a calcination temperature of ~500 °C for synthesizing IrO₂. It is also worth mentioning that, in addition to IrO₂, fluorinated IrO₂ (IrO₂:10F) was also synthesized (using an earlier reported approach¹⁸) for assessment of the electrochemical results.

2.3. Electrocatalyst Material Characterization.

2.3.1. Physicochemical Characterization. X-ray diffraction (XRD) analysis was carried out to acquire qualitative phase information on the as-synthesized electrocatalyst powders. XRD has been performed by using Philips XPRT PRO system, with Cu K α ($\lambda = 0.15406$ nm) radiation at an operating voltage and current of 45 kV and 40 mA, respectively. XRD peak profiles have been analyzed using a pseudo-Voigt function to determine Lorentzian and Gaussian contribution of the peaks.¹⁶ Least-squares refinement techniques have been utilized to evaluate the molar volume and lattice parameters of the as-synthesized electrocatalysts. The textural properties (specific surface area, BJH pore size distribution) of the electrocatalyst powders were derived from a nitrogen adsorption–desorption analysis, and the Brunauer–Emmett–Teller (BET) technique was used to analyze the surface area. The as-synthesized electrocatalyst powders were first vacuum-degassed and then analyzed using a Micromeritics ASAP 2020 instrument. The BET surface area values were obtained using a multipoint BET technique. The electronic conductivity values of the as-synthesized electrocatalyst samples were investigated by utilizing a Jandel Micro position 4-point Probe apparatus (details are given in the Supporting Information). The morphology and microstructure of the electrocatalyst powders have been investigated by performing scanning electron microscopy (SEM). An energy dispersive X-ray spectroscopy (EDX) analyzer (attached with the SEM instrument) was used for the quantitative elemental analysis and to study the distribution of elements by elemental X-ray mapping techniques. The elemental and X-ray mapping analysis of the as-prepared electrocatalyst was carried out using a Philips XL-30FEG system, operated at a voltage of 20 kV. The size and microstructure of the electrocatalyst materials were studied by using a JEOL JEM-2100F transmission electron microscope (TEM) and high-resolution transmission electron microscopy (HRTEM). In addition to EDX analysis, the atomic ratio of Mn and Ir was investigated by using inductively coupled plasma optical emission spectroscopy (ICP-OES, iCAP 6500 duo Thermo Fisher). The electrocatalyst sample was digested with aqua regia at 60 °C for 2 h and then diluted with deionized water before analysis.

X-ray photoelectron spectroscopy (XPS) was carried out to study the element binding and valence states of the electrocatalysts. The XPS analysis was conducted using an ESCALAB 250 Xi system (Thermo Scientific) equipped with a monochromated Al K α X-ray source. The analysis spot of 400 \times 400 μm^2 was well-defined by the microfocused X-ray source. The XPS system functioned in an ultrahigh-vacuum chamber with a base pressure of less than 5×10^{-10} mBar and at room temperature. The binding energy (BE) scale of the analyzer was

calibrated to produce <50 meV deviations of the three standard peaks from their standard values. The aliphatic C 1s peak was observed at 284.6 eV. High-resolution elemental XPS data in the C 2p, S 2p, Mg 2p, and Zn 2p regions were acquired with the analyzer pass energy set to 20 eV (corresponding to energy resolution of 0.36 eV) and the step size set to 0.1 eV.³ The fitting of the elemental spectra was carried out on the basis of calibrated analyzer transmission functions and Scofield sensitivity factors. The effective attenuation lengths for photoelectrons from the standard TPP-2M formalism was achieved using the Avantage software package (Thermo Fisher Scientific). During the fitting of the XPS spectra, fitting parameters such as L/G mix, tail mix, tail height, and tail exponent were fixed at 30%, 100%, 0%, and 0%, respectively. All of the XPS spectra in the present study were fitted symmetrically with Gaussian–Lorentzian functions without introducing any constraints. The wetting characteristics of as-synthesized electrocatalysts were investigated by using an AST Products VCA 2000 video contact angle goniometer. In static water contact angle measurements, a water droplet (10 μL) was vertically dropped onto the electrode surface and the contact angle was detected by the sensitive drop method by drawing a tangent to the edge of the droplet and intersecting it with the measurement baseline.

2.3.2. Electrochemical Characterization. The electrochemical characterization of the as-prepared electrodes has been carried out in a three-electrode configuration using a VersaSTAT 3 (Princeton Applied Research) electrochemical workstation. Sulfuric acid (1 N, H₂SO₄) was used as the electrolyte solution and also as a proton source for the oxygen evolution reaction (OER), maintained at a constant temperature of 40 °C using a Fisher Scientific 910 Isotemp refrigerator circulator during the electrochemical characterization. The oxygen from the electrolyte solution was expelled by purging the electrolyte solution with ultrahigh-purity (UHP) argon gas (Matheson) for ~10 min prior to electrochemical testing. In order to prepare the working electrodes (WEs), electrocatalyst inks of different compositions were produced by using 85 wt % electrocatalyst powder and 15 wt % Nafion 117 (5 wt % solution in lower aliphatic alcohols, Aldrich). The resulting electrocatalyst inks were subjected to sonication for 1 h. After sonication, the catalyst inks were homogenized using a Tissuemiser (Fisher Scientific) for ~3 min and then uniformly spread on the titanium (Ti) foils (Alfa Aesar) followed by drying under ambient conditions. The digital images of electrocatalyst ink coated electrodes are depicted in Figure S1 in the Supporting Information. Pt wire (Alfa Aesar, 0.25 mm thick, 99.95%) was used as the counter electrode (CE), and a mercury/mercurous sulfate (Hg/Hg₂SO₄) electrode (XR-200, Hach) having a potential of +0.65 V with respect to the reversible hydrogen electrode (RHE) was used as the reference electrode (RE). The electrochemical performance of the as-synthesized electrocatalysts for the OER (total electrocatalyst loading 0.3 mg cm⁻²) has been compared with that of an in house synthesized IrO₂ electrocatalyst (total loading 0.3 mg cm⁻²) under identical operating conditions. The potential values reported in this study have been determined and reported with respect to the reversible hydrogen electrode (RHE) and calculated from the formula

$$E_{\text{RHE}} = E_{\text{Hg}/\text{Hg}_2\text{SO}_4} + E^{\circ}_{\text{Hg}/\text{Hg}_2\text{SO}_4} + 0.059\text{pH}$$

where E_{RHE} is the potential versus RHE and $E_{\text{Hg}/\text{Hg}_2\text{SO}_4}$ is the potential measured against the Hg/Hg₂SO₄ reference electrode.

$E^{\circ}_{\text{Hg}/\text{Hg}_2\text{SO}_4}$ is the standard electrode potential of the Hg/Hg₂SO₄ reference electrode (+0.65 V vs RHE).

2.3.2.1. Electrochemical Impedance Spectroscopy (EIS). In order to determine the ohmic resistance (R_{Ω}) and the charge transfer resistance (R_{ct}) of the as-synthesized electrocatalysts, electrochemical impedance spectroscopy (EIS) has been carried out. EIS was conducted using an electrochemical workstation (Versa STAT 3, Princeton Applied Research) in 1 N H₂SO₄ electrolyte solution maintained at 40 °C and at ~1.45 V (which is the typical potential used for assessing the electrochemical activity of the electrocatalysts for the OER). EIS has been operated in the frequency range of 100 mHz to 100 kHz (amplitude 10 mV). The ZView software from Scribner Associates employing the equivalent circuit model given as $R_s(R_e Q_1)(R_{ct} Q_{dl})$ in which R_s (solution resistance) is in series with the parallel combination of the R_e (electrode resistance) and Q_1 (constant phase element) and further in series with the parallel combination of the R_{ct} (surface charge transfer) and Q_{dl} (contribution from double-layer capacitance and pseudo capacitance). The ohmic resistance ($R_{\Omega} = R_s + R_e$) obtained from the EIS was further used for iR_{Ω} correction in the polarization curves of as-prepared electrocatalysts. It should be noted that the $R_s(R_e Q_1)(R_{ct} Q_{dl})$ equivalent circuit model was utilized for the impedance characterization of as-synthesized (Mn_{0.8}Ir_{0.2})O₂ and (Mn_{0.8}Ir_{0.2})O₂:10F NRs, whereas following the previous report¹⁸ of the powder IrO₂ electrocatalyst the $R_s(R_{ct} Q_{dl})$ model in which R_s (solution/ohmic resistance) is in series with the parallel combination of R_{ct} and Q_{dl} was suitably used for EIS fits for the as-synthesized IrO₂ and MnO₂.

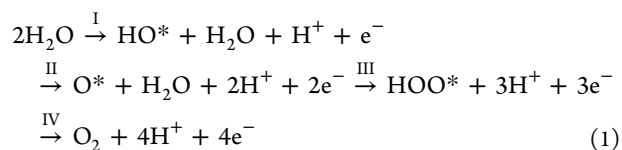
2.3.2.2. Linear Sweep Voltammetry (LSV). The electrocatalytic activity of the as-synthesized electrocatalysts for the OER was analyzed by conducting LSV measurements in 1 N H₂SO₄ electrolyte solution with a scan rate of 10 mV s⁻¹ at 40 °C. The experimentally obtained polarization curves of electrocatalysts having different compositions were iR_{Ω} corrected (R_{Ω} , the ohmic resistance, was determined from the EIS analysis). The onset potential is defined as the potential where the initiation of current inflection is observed in the polarization curve. To compare the electrocatalytic activity of the as-prepared electrocatalysts, the current density at a particular potential of ~1.45 V (which is the typical potential selected for comparison of activity) in iR_{Ω} corrected polarization curves was used. In order to investigate the intrinsic catalytic activity, the obtained current density values are normalized to the BET as well as electrochemical active surface area (ECSA) values. It should be noted that the current density values referenced to geometric surface area (1 cm²), BET surface area, and ECSA are denoted as mA cm⁻²_{geo}, mA cm⁻²_{BET}, and mA cm⁻²_{ECSA}, respectively. To obtain qualitative mechanistic insights into the as-synthesized electrocatalysts, Tafel plots were developed after iR_{Ω} correction using the equation $\eta = a + b \log i$ (i.e., plot of overpotential (η) vs log current ($\log i$)). In this equation, a and b represent the exchange current density and Tafel slope, respectively. Further, the electrochemical active surface area (ECSA) of the as-prepared electrocatalysts was examined by recording the cyclic voltammetry (CV) curves with various scan rates (10, 30, 50, and 70 mV s⁻¹) in the potential range from 0.1 to 1.2 V (vs RHE). The C_{dl} (mF cm⁻²) values were obtained from the slope, i.e. from a plot of differences in current density ($j_{\text{anode}} - j_{\text{cathode}}$) at 0.7 V (vs RHE) vs scan rate. The detailed calculation of ECSA (m² g⁻¹) is described in the Supporting Information. In addition, the intrinsic OER activity of as-prepared electrodes was evaluated by calculating the

specific activity, mass activity, turnover frequency (TOF), and normalization of current densities by ECSA and BET surface area (m² g⁻¹) (see the Supporting Information for calculation details).

2.3.2.3. Electrochemical Stability Test. In order to evaluate the electrocatalytic stability of the as-synthesized electrocatalysts for long-term operation, chronoamperometry (CA) tests (current vs time) have been carried out wherein the electrode was maintained for 24 h in the electrolyte solution of 1 N H₂SO₄ at 40 °C under a constant voltage of ~1.45 V. Further, to investigate the amount of Ir and/or Mn leached out from the working electrode during OER operation, the electrolyte solutions collected after 24 h of CA tests were subjected to elemental analysis by inductively coupled plasma optical emission spectroscopy (ICP-OES, iCAP 6500 duo Thermo Fisher). In addition, ICP-OES analysis was conducted on the electrode following the post-stability tests to investigate the Mn:Ir ratio. Furthermore, in order to assess the structural stability and robustness of as-prepared electrodes, poststability characterizations such as phase (XRD), morphology (SEM), and electronic/surface oxidation state (XPS) analysis were conducted on the electrodes tested for 24 h of chronoamperometry tests.

It should also be noted that all the experiments reported in the present study were repeated and analyzed with at least three repeats and the data are reported as the average of three independently generated as-prepared electrocatalyst samples.

2.4. Computational Methodology. The overall electrocatalytic activity and the overpotential of the (Mn, Ir)O₂:F OER electrocatalyst is anticipated to depend on the electronic and crystal structure of the catalyst material as well as the thermodynamics of the four elementary steps of the oxygen evolution reaction (eq 1).



wherein the asterisk represents an active site on the metal oxide surface.⁵³ As will be described in Results and Discussion of the present study, the as-synthesized (Mn, Ir)O₂:F NRs exhibit a tetragonal crystal form analogous to the α -MnO₂ structure with tetragonal symmetry and the space group $I4/m$ (No. 87).³⁹ The crystal structure of α -MnO₂ shown in Figure 1b–d will be utilized to study the influence of compositions on the electronic structure as well as the onset potential and structural stability in the computational component of the current study. Herein, the following compositions with an α -MnO₂ structure have been considered in the computational study: pure MnO₂, (Mn_{0.75}Ir_{0.25})O₂, and F-doped (Mn_{0.75}Ir_{0.25})O_{2-x}F_x with $x = 0.25, 0.625, 1.0$. Such F-doped formula units correspond approximately to 4, 10, and 15 wt % of F. These compositions have been chosen on the basis of the elementary unit cell of an α -MnO₂ structure comprised of 8 atoms of Mn and 16 atoms of O.

The free energies (ΔG) of all the four anodic intermediate reactions (I–IV) from eq 1 were utilized to calculate the electrical potentials of a certain specific reaction. Consequently, a systematic analysis of all the calculated free energies may assist in identifying the rate-determining steps (RDS) as well as the corresponding overpotential of the oxygen evolution reaction occurring at the electrochemically active surface. This computational analysis is critical to assess the catalytic activity of the

specific material used as an electrocatalyst in the OER process. For comparison purposes, three different materials have been chosen for calculation of the OER elementary steps: (a) pure MnO_2 , (b) MnO_2 doped with small amount of Ir as a substituent of Mn at the corresponding Mn-type lattice sites, and (c) $(\text{Mn},\text{Ir})\text{O}_2$ doped with F as a substituent of O. For calculations of the total energies, electronic structures, and free energies of the four elementary steps qualitatively characterizing the electrocatalytic activity of the aforementioned oxides, bulk and (110) surface $\alpha\text{-MnO}_2$ structures have been utilized.

For bulk calculations a tetragonal 24-atom unit cell with an $\alpha\text{-MnO}_2$ crystal structure has been selected as the basis for construction of different Ir, Mn, and F concentrations of the solid solution oxides. Such a unit cell contains 8 transition metal atoms and 16 atoms of oxygen/fluorine. Thus, for the convenience of theoretical calculations, the basic compositions without introduction of fluorine have been chosen as follows: pure MnO_2 with 8 Mn and 16 O atoms as well as Ir-doped oxide $(\text{Ir}_{0.25}\text{Mn}_{0.75})\text{O}_2$ with 2 Ir, 6 Mn, and 16 O atoms. For simulation of various dopants of fluorine 2, 5, and 8 atoms of oxygen were randomly replaced with the corresponding number of fluorine atoms, generating the following formula units: $(\text{Mn}_{0.75}\text{Ir}_{0.25})\text{O}_{1.75}\text{F}_{0.25}$, $(\text{Mn}_{0.75}\text{Ir}_{0.25})\text{O}_{1.375}\text{F}_{0.625}$, and $(\text{Mn}_{0.75}\text{Ir}_{0.25})\text{O}_{1.0}\text{F}_{1.0}$, which approximately corresponded to 4, 10, and 15 wt % of F content, respectively. Such compositions have been chosen for all calculations of the bulk and surface electronic structures employed in the present study. For calculation of the (110) surface electronic properties of the materials, a two-dimensional slab of thickness ~ 6.7 Å repeated in the $[1, -1, 0]$ direction with a 24-atom unit cell and a vacuum distance of ~ 13 Å between adjacent images was selected. In order to calculate the free energies of all the elementary reactions, i.e. (I)–(IV) (eq 1), for pure and doped $\alpha\text{-MnO}_2$, the coordinatively unsaturated sites (CUS) located at the (110) surface have been considered as active sites following previous computational studies on similar systems.^{2,19,53,54} All of the intermediate species involved in the OER, i.e. O^* , OH^* , and OOH^* , have been attached to the top surface layer. Three bottom layers of the slab were fixed with the lattice parameter corresponding to the bulk $\alpha\text{-MnO}_2$. Apart from these three bottom layers, all other layers of the slab together with the intermediate species were fully relaxed, which resulted in the residual force components on each atom to be lower than 0.01 eV/(Å atom).

The crystal structure chosen for the calculations in the present study is shown in Figure 1b. Two different atomic positions of Ir as a replacement of Mn at the (110) surface have been considered and marked as Pos.1 and Pos.2 to investigate the difference between the electronic structures of pure and Ir-doped MnO_2 compounds as well as to assess the effects of Mn and Ir on the overpotential of the $(\text{Mn},\text{Ir})\text{O}_2$. The first Ir atomic distribution consists of one Ir atom located in place of Mn just below the CUS shown in Figure 1c,d. The second distribution is characterized by putting Ir atoms at the neighboring position denoted as Pos.2, while the CUS is located above the Mn atom (Figure 1d). Also, to mimic F doping in the electrocatalyst material, one oxygen atom has been replaced by an F atom at the oxygen site adjacent to the CUS at the top layer and is shown in Figure 1c. To measure the free energies of the four elementary reaction steps as discussed above, such atomic distributions at the (110) surface covered by adsorbed oxygen monolayers in combination with intermediate species have been used. For calculation of the total energies, electronic structures, and density of electronic states (DOS) of the studied materials, the

density functional theory (DFT) executed in the Vienna ab initio simulation package (VASP) was utilized within the projector-augmented wave (PAW) method⁵⁵ and the spin-polarized generalized gradient approximation (GGA) for the exchange-correlation energy functional in a form described by PBE (Perdew–Burke–Ernzerhof).^{56,57} This computational package examines the electronic structure, and via the Hellmann–Feynman theorem the interatomic forces are determined from first principles. The standard PAW potentials were employed for the elemental components, and the iridium, manganese, oxygen, and fluorine potentials thus contained nine, seven, six, and seven valence electrons, respectively. Furthermore, to maintain high accuracy for total energy calculations for all of the electrocatalyst compositions, a plane wave cutoff energy of 520 eV has been selected. By utilization of the double-relaxation procedure, the internal positions as well as the lattice parameters of atoms have been entirely optimized.²

Furthermore, in the present study the minima of the total energies with respect to the lattice parameters and internal ionic positions have been evaluated. Also, by minimization of the Hellman–Feynman forces via a conjugate gradient method, a geometry optimization was attained which will cause the net forces applied on every ion in the lattice to be close to zero. The total electronic energies were converged within 10–5 eV/unit cell, which result in the residual force components on each atom to be lower than 0.01 eV/(Å atom). This permits the accurate determination of the internal structural parameters. Herein, the Monkhorst–Pack scheme has been employed to sample the Brillouin zone (BZ) and create the k -point grid for the solids and the different isolated atoms used in the current study. The choice of an appropriate number of k points in the irreducible part of the BZ was made on the basis of the convergence of the total energy to 0.1 meV/atom. It is significant to remark that, for Mn–Ir–O–F compositions, the corresponding atomic distributions are uncertain and thus different spatial configurations can be used for exemplification of the atomic distributions. This uncertainty has been disregarded by assembling the various atomic configurations for each selected composition, and the configurations which correspond to the minimum total energy have been chosen for executing the additional numerical analysis of these specific compositions of the binary oxide electrocatalysts.

3. RESULTS AND DISCUSSION

3.1. Physical Characterization of Electrocatalysts. To characterize the crystal phase and phase purity of as-synthesized electrocatalysts, the powder X-ray diffraction (XRD) patterns of MnO_2 , $(\text{Mn}_{0.8}\text{Ir}_{0.2})\text{O}_2$, $(\text{Mn}_{0.8}\text{Ir}_{0.2})\text{O}_2:10\text{F}$, and IrO_2 are studied and compared in Figure 2. The as-synthesized IrO_2 (Figure 2a) reveals the rutile type tetragonal structure (JCPDS 15-870) with lattice constants of $a = 4.49$ Å and $c = 3.15$ Å and unit cell and molar volume of ~ 63.78 Å³ and 19.20 cm³ mol⁻¹, respectively (Table 1), similar to earlier reports.^{18,58} Figure 2b shows the diffraction patterns of the hydrothermally synthesized MnO_2 . All of the diffraction peaks in Figure 2b can be readily indexed to the pure tetragonal phase of $\alpha\text{-MnO}_2$ (space group $I4/m$ (No. 87), JCPDS 44-0141) with lattice constants $a = 9.784$ Å and $c = 2.852$ Å and unit cell volume of 273 Å³ (Table 1), which is in good agreement with the computationally calculated lattice parameters (Table S1, Supporting Information) as well as earlier studies,^{39,48} indicating the formation of highly pure and crystalline $\alpha\text{-MnO}_2$. The XRD patterns of $(\text{Mn}_{0.8}\text{Ir}_{0.2})\text{O}_2$ and $(\text{Mn}_{0.8}\text{Ir}_{0.2})\text{O}_2:10\text{F}$ are depicted in Figure 2c,d, respectively. The

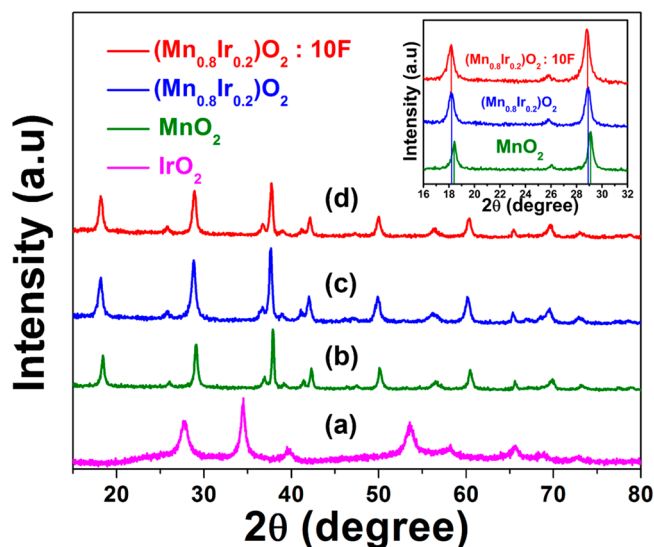


Figure 2. Powder XRD patterns of the as-synthesized (a) IrO₂, (b) MnO₂, (c) (Mn_{0.8}Ir_{0.2})O₂, and (d) (Mn_{0.8}Ir_{0.2})O₂:10F electrocatalysts (inset: magnified view of XRD patterns).

XRD pattern reflections of (Mn_{0.8}Ir_{0.2})O₂ and (Mn_{0.8}Ir_{0.2})O₂:10F correspond to that of the tetragonal structure of α -MnO₂ (Figure 2b). The Ir and/or F-doped MnO₂ did not demonstrate the presence of any secondary phase of Mn-, Ir-, or F-based compounds, which can be attributed to the incorporation of dopants into the MnO₂ lattice. Herein, it is worth mentioning that the magnified XRD patterns of our as-synthesized (Mn, Ir)O₂ samples (inset of Figure 2) did not feature any characteristic amorphous hump at a 2θ peak position of $\sim 22^\circ$ which is typically observed in the XRD pattern of amorphous IrO₂, which further affirms the incorporation of Ir into the crystalline MnO₂ lattice.^{59,60} This result has been substantiated by the change in the lattice parameters and molar volumes of the Ir- and F-incorporated MnO₂ samples. As shown in the inset of Figure 2, close inspection of the XRD patterns of (Mn_{0.8}Ir_{0.2})O₂ and (Mn_{0.8}Ir_{0.2})O₂:10F indicated that the XRD peaks of these synthesized solid solution electrocatalysts are slightly shifted toward a lower angle by a 2θ value of $\sim 0.3^\circ$. This negative shift in 2θ positions clearly suggests the lattice expansion⁶¹ of (Mn_{0.8}Ir_{0.2})O₂ and (Mn_{0.8}Ir_{0.2})O₂:10F, which is primarily instigated by the incorporation of Ir into the MnO₂ crystalline framework (Table 1). This lattice expansion can be attributed to the difference in ionic radii between the host element (Mn⁴⁺ 0.54 Å)⁶² and the dopant solute ion (Ir⁴⁺ 0.62 Å).⁶³ Furthermore, the increased lattice parameters and unit cell volume of (Mn_{0.8}Ir_{0.2})O₂ (278.44 Å³) and (Mn_{0.8}Ir_{0.2})O₂:10F (278.47 Å³) evidently suggest the successful incorporation of dopant ions (Ir⁴⁺) into the host MnO₂ framework (Table 1). It is worth mentioning that the as-synthesized (Mn_{0.8}Ir_{0.2})O₂ and (Mn_{0.8}Ir_{0.2})O₂:10F exhibited comparable lattice parameters and

molar volume (Table 1), suggesting that F doping in the O²⁻ sites has no significant effect on the molar volume of (Mn_{0.8}Ir_{0.2})O₂:10F. This can be ascribed to the comparable ionic radii of O²⁻ (1.25 Å) and F⁻ (1.20 Å).¹⁶ This result conforms well with various F-substituted solid solution oxide electrocatalysts as reported in earlier studies.^{2,16,21} Furthermore, the as-synthesized IrO₂:10F (Figure S2a, Supporting Information) and MnO₂:10F (Figure S2b) exhibited XRD reflections similar to those of their respective parent electrocatalyst structures. These results suggest that fluorinated IrO₂ and MnO₂ demonstrate the formation of a solution devoid of any undesirable phase separation and/or mixed-phase formation due to F incorporation. Herein, it is worth mentioning that, as elucidated in Preparation of Electrocatalyst Materials, α -MnO₂ initiates its transformation from the α -MnO₂ to the α -Mn₂O₃ phase beyond the calcination temperature of 500 °C (typically 600–800 °C).^{47,49} Thus, as can be seen from the XRD pattern of α -MnO₂ calcined at 400 °C (Figure S2c, Supporting Information), any possibilities of structure degradation in the α -MnO₂-based electrocatalysts synthesized at 400 °C are clearly eliminated.

Furthermore, the Brunauer–Emmett–Teller (BET) based specific surface areas (SSAs) of as-synthesized MnO₂, (Mn_{0.8}Ir_{0.2})O₂, (Mn_{0.8}Ir_{0.2})O₂:10F and IrO₂ derived from the N₂ adsorption–desorption analysis are given in Table 1 and depicted in Figure 3. According to the International Union of Pure and Applied Chemistry (IUPAC) classification, the N₂-adsorption isotherms of these materials (Figure 3) exhibit a type IV shape with H3 hysteresis loop, similar to the previous reports of MnO₂ nanorods, indicating that the as-synthesized materials possess a slit-shaped mesoporous structure (as also witnessed from the Barrett–Joyner–Halenda (BJH) pore size distribution results shown in Figure S3 and Table S2, Supporting Information). Such a mesoporous nature is indeed beneficial for achieving facile electrolyte penetration by offering efficient transport pathways to the interior voids of the electrocatalyst surface.^{64,65} The measured BET surface areas of the pure MnO₂ and (Mn_{0.8}Ir_{0.2})O₂ were ~ 3.72 and ~ 3.70 m² g⁻¹, respectively. These comparable BET surface area values suggest that the Ir incorporation has a negligible effect on the BET surface area of MnO₂. However, (Mn_{0.8}Ir_{0.2})O₂:10F exhibited a BET surface area (~ 3.55 m² g⁻¹) slightly lower than those of MnO₂ and (Mn_{0.8}Ir_{0.2})O₂. Such a decrease in surface area of fluorinated (Mn_{0.8}Ir_{0.2})O₂ can be attributed to the exothermic phenomenon of NH₄F (i.e., fluorine precursor) burning during the calcination of (Mn_{0.8}Ir_{0.2})O₂:10F NRs, which may lead to an increase in the size of (Mn_{0.8}Ir_{0.2})O₂:10F NRs, causing a reduction in the BET surface area. Similar behavior regarding the decrease in BET surface area with incorporation of F has been observed in various reported studies.¹⁸ The as-synthesized IrO₂ exhibited a significantly higher BET surface area of ~ 189 m² g⁻¹, comparable to that in an earlier report.¹⁸

Table 1. Lattice Parameter, Volume, and BET Surface Area of As-Synthesized Electrocatalysts

electrocatalyst composition	lattice parameter (Å)		volume		BET surface area (m ² g ⁻¹)
	$a = b$	c	unit cell (Å ³)	molar (cm ³ mol ⁻¹)	
MnO ₂	9.784	2.852	273.012	20.55	3.72
(Mn _{0.8} Ir _{0.2})O ₂	9.831	2.881	278.44	20.96	3.70
(Mn _{0.8} Ir _{0.2})O ₂ :10F	9.835	2.879	278.47	20.96	3.55
IrO ₂	4.49	3.15	63.78	19.20	189

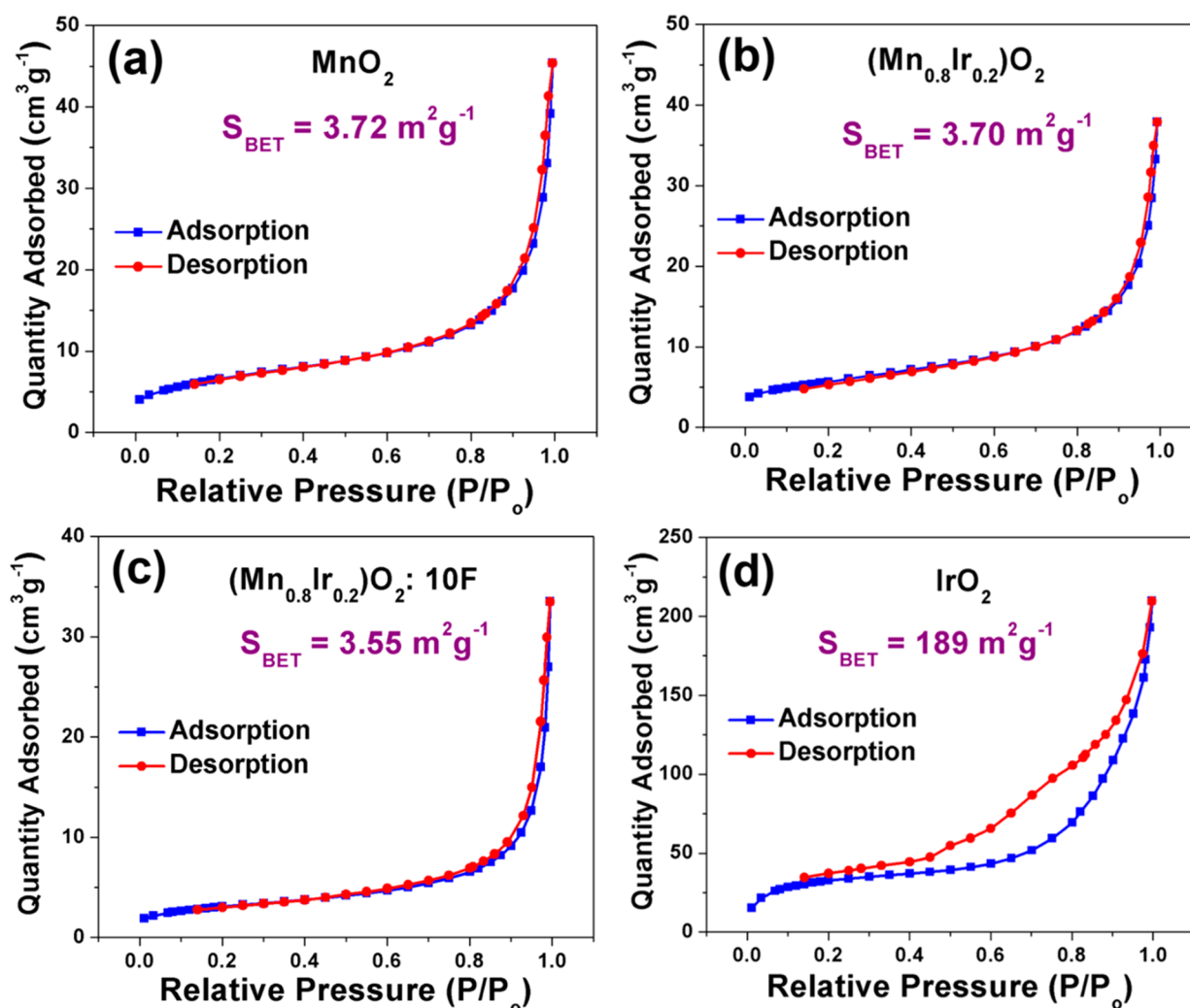


Figure 3. N_2 adsorption–desorption isotherms of the as-synthesized (a) MnO_2 , (b) $(Mn_{0.8}Ir_{0.2})O_2$, (c) $(Mn_{0.8}Ir_{0.2})O_2:10F$, and (d) IrO_2 .

Figure 4 depicts the scanning electron microscope (SEM) images of as-synthesized α - MnO_2 , $(Mn_{0.8}Ir_{0.2})O_2$, and $(Mn_{0.8}Ir_{0.2})O_2:10F$ electrocatalyst powders. As shown in Figure 4a–c, the as-synthesized MnO_2 possesses highly dense, well-spaced, and randomly aligned uniform one-dimensional (1D) rod shape morphology. The 1D MnO_2 rods exhibited a diameter of ~ 40 – 50 nm and length ranging from ~ 0.5 to 3 μm throughout the catalyst material, clearly indicating the attainment of high aspect ratios (L/D) for the as-synthesized nanorods (NRs). Further, as can be seen from the SEM micrographs of $(Mn_{0.8}Ir_{0.2})O_2$ (Figure 4d–f) and $(Mn_{0.8}Ir_{0.2})O_2:10F$ (Figure 4g–i), they demonstrate similar nanorod motifs with nanoscale diameter (~ 40 – 50 nm) and diverse lengths. In addition, $(Mn_{0.8}Ir_{0.2})O_2$ and $(Mn_{0.8}Ir_{0.2})O_2:10F$ electrocatalysts show a similar well-spaced nanorod structure, which is beneficial for attaining the rapid release of oxygen bubbles during the OER process.³ These SEM results evidently suggest that the nanorod architecture of pure MnO_2 is well preserved after incorporation of Ir and F and formation of the homogeneous solid solution with MnO_2 during the calcination process. Furthermore, the energy dispersed X-ray spectroscopy (EDX) elemental mapping images of $(Mn_{0.8}Ir_{0.2})O_2:10F$ (Figure S4a, Supporting Information) confirm the homogeneous distribution of elements within as-synthesized nanorods, suggesting the formation of a highly pure solid solution, without the presence of any undesired

impurity from the precursors as well as segregation of the species at any specific region. In addition, the quantitative elemental analysis derived from the EDX spectrum of $(Mn_{0.8}Ir_{0.2})O_2:10F$ NRs (Figure S4b) indicated the atomic ratio of Mn and Ir as 80.24:19.76, which is in good agreement with the ICP-OES results as well as the selected nominal composition (Mn:Ir = 80:20). In addition, the EDX elemental mapping images (Figure S4c) and EDX spectrum (Figure S4d) of IrO_2 also demonstrate the uniform dispersion of elements within the as-synthesized catalyst particles.

The morphology of the $(Mn_{0.8}Ir_{0.2})O_2:10F$ NRs was further examined by transmission electron microscopy (TEM). As can be seen from Figure 5a,b, the $(Mn_{0.8}Ir_{0.2})O_2:10F$ electrocatalyst dispersed on the TEM grid demonstrated the typical rod-shaped morphology with a diameter of ~ 40 nm. The high-resolution transition electron microscopy (HRTEM) images of $(Mn_{0.8}Ir_{0.2})O_2:10F$ NR (Figure 5c,d) show a distinguishable and well-resolved uniform lattice fringe space of ~ 0.6954 nm, corresponding to the (110) crystallographic planes of $(Mn_{0.8}Ir_{0.2})O_2:10F$. In addition, from the HRTEM image of MnO_2 (Figure S4e), the lattice fringe space corresponding to the (110) crystallographic plane of α - MnO_2 was obtained as ~ 0.6890 nm, which is indeed in good agreement with that of the XRD results. The larger lattice fringe of $(Mn_{0.8}Ir_{0.2})O_2:10F$ (~ 0.6954 nm) in comparison to that of α - MnO_2 (~ 0.6890

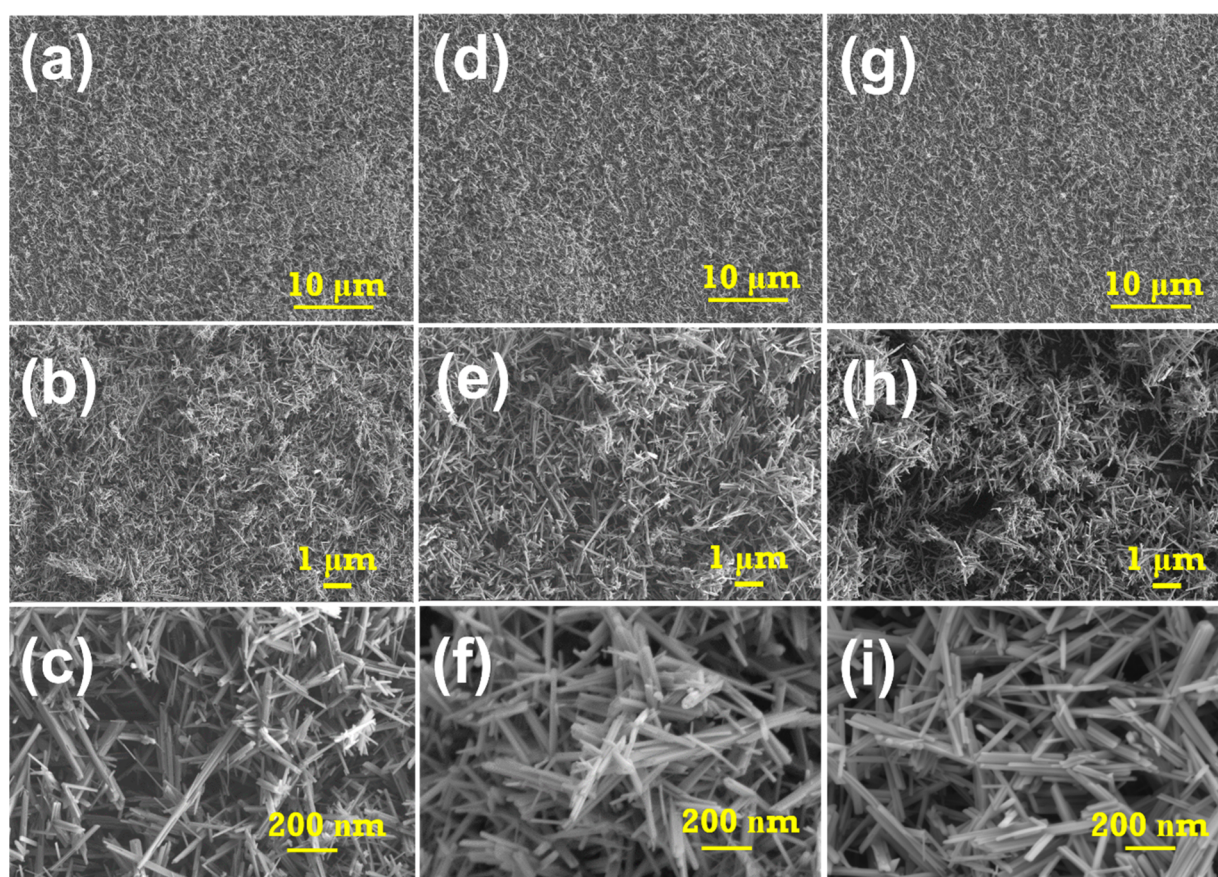


Figure 4. (a) SEM micrographs of the as-synthesized (a–c) MnO_2 , (d–f) $(\text{Mn}_{0.8}\text{Ir}_{0.2})\text{O}_2$, and (g–i) $(\text{Mn}_{0.8}\text{Ir}_{0.2})\text{O}_2:10\text{F}$ NRs.

nm)³⁹ evidently shows lattice expansion due to Ir incorporation into the MnO_2 crystalline lattice. As already discussed in the XRD results, this lattice expansion can be attributed to the difference in ionic radii between the host element (Mn^{4+} 0.54 Å)⁶² and the dopant solute ion (Ir^{4+} 0.62 Å).⁶³ Furthermore, a line scan analysis of the $(\text{Mn}_{0.8}\text{Ir}_{0.2})\text{O}_2:10\text{F}$ NR (Figure 5e) was undertaken to confirm the homogeneous dispersion of Mn and Ir within the as-synthesized $(\text{Mn}_{0.8}\text{Ir}_{0.2})\text{O}_2:10\text{F}$ NR. In addition, Figure 5f illustrates the EDX elemental mapping images of Mn, Ir, and O for the $(\text{Mn}_{0.8}\text{Ir}_{0.2})\text{O}_2:10\text{F}$ NR, suggesting the uniform spatial distribution of these elements over the examined surface of $(\text{Mn}_{0.8}\text{Ir}_{0.2})\text{O}_2:10\text{F}$ NR, lacking any segregation of elements at any specific site. Thus, in addition to XRD results, taken together, these EDX and line scan analysis results justified the formation of a single-phase homogeneous solid solution of MnO_2 and IrO_2 (i.e., $(\text{Mn}_x\text{Ir}_{1-x})\text{O}_2:\text{F}$). Moreover, the EDX elemental analysis conducted on the $(\text{Mn}_{0.8}\text{Ir}_{0.2})\text{O}_2:10\text{F}$ NR (Figure S4f) is in a good agreement with the particular nominal composition of Mn and Ir.

The chemical valence states of Mn, Ir, and O in the as-synthesized MnO_2 , $(\text{Mn}_{0.8}\text{Ir}_{0.2})\text{O}_2$, $(\text{Mn}_{0.8}\text{Ir}_{0.2})\text{O}_2:10\text{F}$ electrocatalysts were investigated by employing X-ray photoelectron spectroscopy (XPS). Figure 6 displays the XPS spectra of Mn, Ir, and O for MnO_2 , $(\text{Mn}_{0.8}\text{Ir}_{0.2})\text{O}_2$, and $(\text{Mn}_{0.8}\text{Ir}_{0.2})\text{O}_2:10\text{F}$ NRs, respectively. The XPS spectrum of Mn 2p (Figure 6a) of the as-prepared $\alpha\text{-MnO}_2$ reveals two peaks located at binding energy values of ~ 642 and ~ 653.8 eV, which are attributed to the Mn $2p_{3/2}$ and Mn $2p_{1/2}$ doublet, respectively, with a spin-energy separation of 11.8 eV (similar to earlier reports).^{2,66} As can be seen from Figure 6a, in the XPS spectrum of Mn 2p, an

additional peak was observed at ~ 646 eV, similar to previous XPS reports of Mn, which can be considered as a shakeup or satellite peak.^{67,68} The XPS spectrum of $(\text{Mn}_{0.8}\text{Ir}_{0.2})\text{O}_2$ exhibited the presence of an Mn $2p_{3/2}$ and Mn $2p_{1/2}$ doublet with binding energy values comparable to those of pure MnO_2 . However, it is interesting to note that the peak positions of the Mn $2p_{3/2}$ and Mn $2p_{1/2}$ doublet of $(\text{Mn}_{0.8}\text{Ir}_{0.2})\text{O}_2:10\text{F}$ exhibited a significant positive shift of $\sim 0.7\text{--}0.9$ eV toward higher binding energy in comparison to those of pure MnO_2 and $(\text{Mn}_{0.8}\text{Ir}_{0.2})\text{O}_2$, which is consistent with the previously reported XPS results of F-doped solid solution electrocatalyst systems (Table S3a, Supporting Information).^{2,16,20} This positive shift in binding energy indicates the beneficial binding of F in the $(\text{Mn}_{0.8}\text{Ir}_{0.2})\text{O}_2:10\text{F}$ NRs, which is attributable to the modification of the electronic structure (details are in the Computational Study Results) of $(\text{Mn}_{0.8}\text{Ir}_{0.2})\text{O}_2:10\text{F}$ as a result of the solid solution formation and incorporation of F, leading to stronger binding due to the higher electronegativity of F.² Furthermore, the Mn:Ir ratio in the XPS analysis of $(\text{Mn}_{0.8}\text{Ir}_{0.2})\text{O}_2:10\text{F}$ was obtained as 80.17:19.83, which is in good agreement with the nominal composition as well as EDX results, suggesting the presence of Mn and Ir in a nominal composition ratio (80:20) on the surface as well as in the bulk of the as-synthesized $(\text{Mn}_{0.8}\text{Ir}_{0.2})\text{O}_2:10\text{F}$ NRs and thus, negates the possibility of only surface modification of MnO_2 NRs or Ir richness via segregation occurring at the surface of MnO_2 NRs due to Ir incorporation. It should be noted that, following the comprehensive XPS studies by the Schlogl and Morgan group in the literature,^{69–71} the XPS plot details of binding energies (eV), full width at half-maximum (fwhm), and spin-energy separation (ΔS) are provided in Table S3.

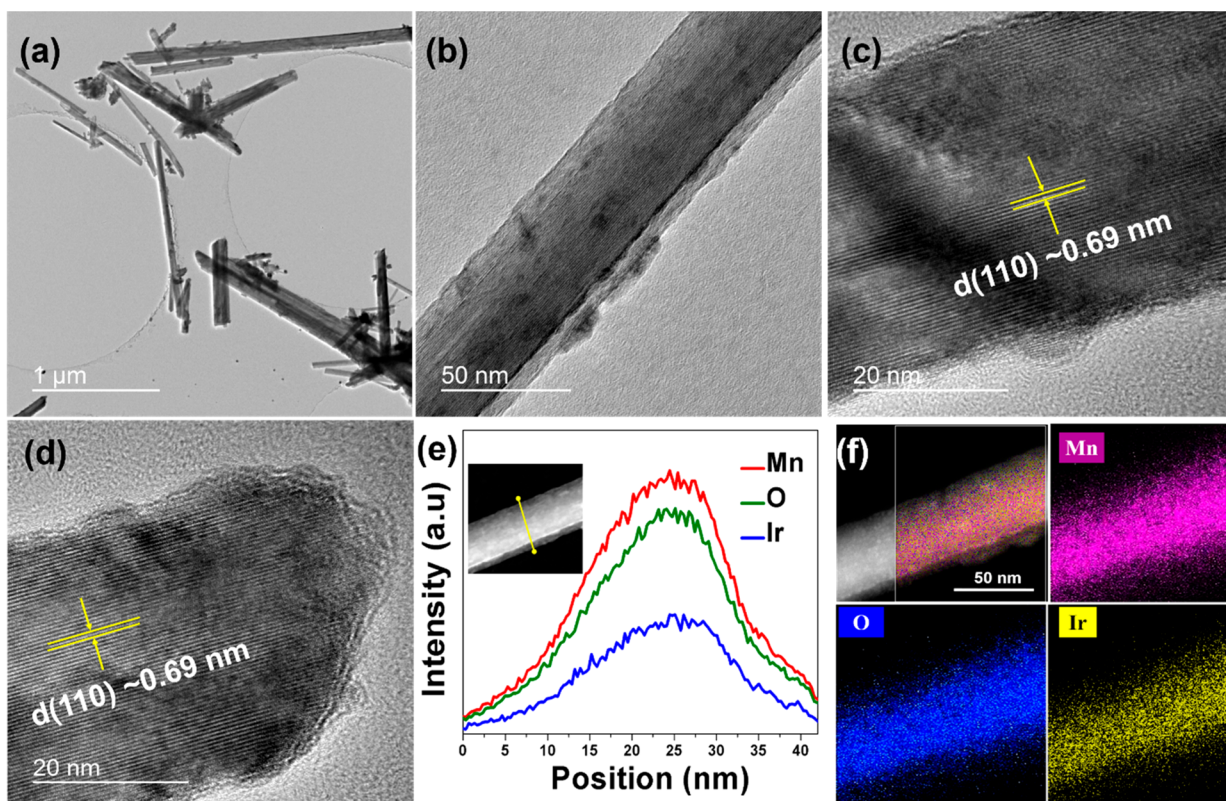


Figure 5. (a, b) TEM images of as-synthesized $(\text{Mn}_{0.8}\text{Ir}_{0.2})\text{O}_2:10\text{F}$ NRs, (c, d) HRTEM images of a representative $(\text{Mn}_{0.8}\text{Ir}_{0.2})\text{O}_2:10\text{F}$ NR, highlighting a lattice fringe of ~ 0.69 nm that corresponds to the (110) plane, (e) line scan analysis across a representative $(\text{Mn}_{0.8}\text{Ir}_{0.2})\text{O}_2:10\text{F}$ NR, and (f) EDX elemental mapping of Mn, O, and Ir of the $(\text{Mn}_{0.8}\text{Ir}_{0.2})\text{O}_2:10\text{F}$ NR.

Figure 6b shows the high-resolution XPS spectra of Ir for IrO_2 , $(\text{Mn}_{0.8}\text{Ir}_{0.2})\text{O}_2$, and $(\text{Mn}_{0.8}\text{Ir}_{0.2})\text{O}_2:10\text{F}$ electrocatalysts, respectively. The XPS spectrum of Ir in IrO_2 and $(\text{Mn}_{0.8}\text{Ir}_{0.2})\text{O}_2$ displays the presence of an Ir $4f_{7/2}$ and Ir $4f_{5/2}$ doublet corresponding to binding energies of ~ 61.8 and 64.9 eV, respectively.^{2,72} In the case of $(\text{Mn}_{0.8}\text{Ir}_{0.2})\text{O}_2:10\text{F}$, a similar behavior of positive shift (~ 0.8 eV) in binding energy values for the Ir $4f$ doublet positions was witnessed, which can again be ascribed to the modification of the electronic structure of $(\text{Mn}_{0.8}\text{Ir}_{0.2})\text{O}_2:10\text{F}$ upon F-substituted solid solution formation. It is also worth mentioning that, in the present XPS study, the Ir $4f_{7/2}:\text{Ir } 4f_{5/2}$ intensity ratios (for symmetrical peak shapes) were obtained in the range of $\sim 1.22:1$ to $\sim 1.26:1$, which is in rational agreement with the theoretical value of $1.33:1$.⁷⁰ Furthermore, the spin-orbit splitting of Ir $4f_{5/2}$ and Ir $4f_{7/2}$ was obtained as ~ 3.1 eV (Table S3b, Supporting Information), which is again in very good agreement with the (symmetrical or asymmetrical) peak separation constraint of 3 eV, as witnessed in the various published XPS reports.^{70,73} In addition, the fitting of the Ir $4f$ components with the unusual asymmetric core-electron line shapes in the metallic oxide IrO_2 is well-documented in the literature. However, in the literature, there are also Ir oxide based electrocatalyst systems such as pure IrO_x as well as doped IrO_x ($\text{IrNi}@\text{IrO}_x$)⁷⁵ wherein the less asymmetric or lack of asymmetric nature has been evidently witnessed, similarly to the presently observed Ir $4f$ results. According to Strasser and co-workers,⁷⁵ the pronounced symmetric nature of these components can be attributed to the formation of surface hydroxide or potentially numerous defects generated during the electrocatalyst synthesis.

Next, as shown in Figure 6c, a dominant peak for O 1s at a binding energy of ~ 530.1 eV was observed for MnO_2 and IrO_2 , which corresponded to the metal-oxygen bond.⁷² Similarly, the deconvoluted O 1s spectra of $(\text{Mn}_{0.8}\text{Ir}_{0.2})\text{O}_2$ and $(\text{Mn}_{0.8}\text{Ir}_{0.2})\text{O}_2:10\text{F}$ also exhibited dominant peaks at ~ 530.1 and ~ 530.8 eV, respectively (Table S3c). Herein, as can be seen from deconvoluted O 1s spectra of $(\text{Mn}_{0.8}\text{Ir}_{0.2})\text{O}_2$ and $(\text{Mn}_{0.8}\text{Ir}_{0.2})\text{O}_2:10\text{F}$, shoulder peaks centered at ~ 531.8 and 532.3 eV, respectively, were detected. As reported in various studies, this shoulder peak at the higher binding energy is attributed to the high binding energy component (HBEC) developed due to oxygen deficiencies or vacancies within the solid solution framework.⁷⁶⁻⁷⁸ Herein, a similar positive shift in binding energy value for O 1s was observed for F-containing $(\text{Mn}_{0.8}\text{Ir}_{0.2})\text{O}_2$, clearly indicating the beneficial effect of the F substitution. However, the presence of F could not be unequivocally determined by XPS and EDX analysis, which is similar to the case for the various F-doped solid solution electrocatalyst systems reported in previous studies.^{2,16,20} Nonetheless, as elucidated in the above XPS discussions, the positive shifts in the binding energy values for Mn 2p, Ir 4f, and O 1s indicate the attainment of stronger binding due to the higher electronegativity of fluorine incorporated into the solid solution electrocatalyst lattice. This result is in good agreement with the various XPS studies on F-doped SnO_2 , MnO_2 , Nb_2O_5 , RuO_2 , IrO_2 etc. as solid solution electrocatalysts.^{2,17,21} In light of this XPS discussion of F, various researchers (Shaltout et al.,⁷⁹ Amanullah et al.,⁸⁰ Datta et al.¹⁶) have postulated that the low concentration of F (or the fluorine content is lower than the detection limit of XPS^{79,80}) in the as-synthesized material can be attributed to the absence of an F 1s peak. Similar experimental

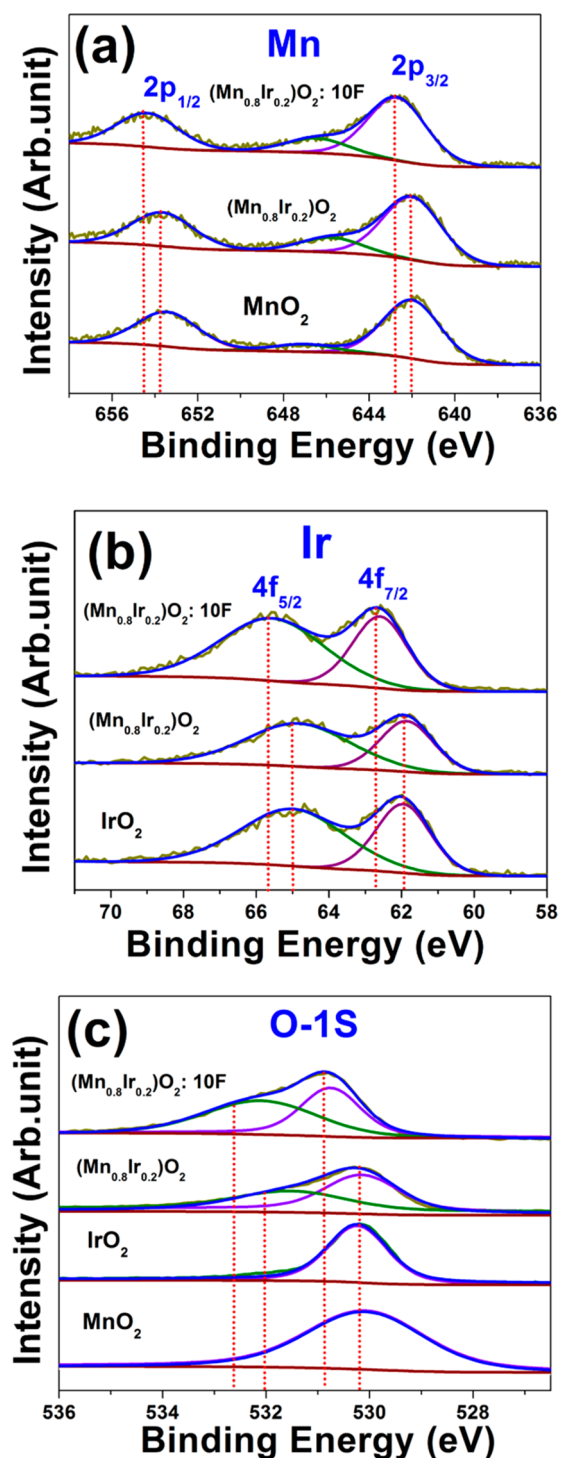


Figure 6. XPS spectra of (a) Mn 2p, (b) Ir 4f, and (c) O 1s for the as-synthesized electrocatalysts.

observations and difficulties in detecting fluorine by either XPS techniques or Auger electron spectroscopy (AES) have been mentioned by other researchers.^{79,81} Nonetheless, in the study conducted by Sun et al.,⁸² the presence of an F 1s XPS spectrum has been detected at a higher (18 wt %) F content in carbon black. In any event, the presence of F in the as-synthesized $(\text{Mn}_{0.8}\text{Ir}_{0.2})\text{O}_2:10\text{F}$ NRs has been detected by solid-state NMR spectroscopy (see Figure S5, Supporting Information, for the NMR analysis result).

Further, the static contact angle method by using a water droplet (10 μL) was employed to investigate the wetting characteristics of the as-synthesized electrocatalyst nanorods deposited on the Ti substrate (current collector). In the absence of any electrocatalyst coating, the bare Ti foil exhibited an average water contact angle of $\sim 127 \pm 1.07^\circ$ (Figure 7a) (which is in good agreement with the water contact angle measurements reported for Ti/titania foils⁸³), suggesting a highly hydrophobic nature for the aqueous electrolyte. In contrast, MnO_2 NRs coated on Ti foil (MnO_2/Ti) exhibited a good hydrophilic nature with a significantly lower average water contact angle of $\sim 47 \pm 0.67^\circ$ (Figure 7b), reflecting close agreement with the previously reported values.⁸⁴ This hydrophilic behavior can be attributed to various factors such as hydroxyl (OH^-) group interaction of Mn atoms with the constitutional water within the as-synthesized MnO_2 powder.^{84–86} Also, the mesoporous nature of the as-synthesized MnO_2 (as witnessed from the BET adsorption isotherm, Figure 3) is indeed beneficial for achieving an electrode–electrolyte interaction, which certainly improves the wettability of the electrode surface. In addition, the hydrophilic domain containing an $-\text{SO}_3^-$ group in Nafion (used as a binder to prepare the catalyst ink) is also well-known for its efficient water adsorption properties and can be another possible contributor to enhancing the wetting characteristics of the surface of the MnO_2 electrode.^{87–89} The contact angle value of MnO_2 ($\sim 47^\circ$) was noticeably influenced when the $(\text{Mn}_{0.8}\text{Ir}_{0.2})\text{O}_2$ and $(\text{Mn}_{0.8}\text{Ir}_{0.2})\text{O}_2:10\text{F}$ electrocatalysts were coated on the Ti foil. Interestingly, $(\text{Mn}_{0.8}\text{Ir}_{0.2})\text{O}_2$ (Figure 7c) and $(\text{Mn}_{0.8}\text{Ir}_{0.2})\text{O}_2:10\text{F}$ (Figure 7d) coatings on Ti foil exhibited significantly reduced average contact angles of $\sim 20 \pm 0.82$ and $18 \pm 0.54^\circ$, respectively, indicating their excellent hydrophilic nature. These decreased contact angle values evidently suggest that the nanorods of $(\text{Mn}_{0.8}\text{Ir}_{0.2})\text{O}_2$ and $(\text{Mn}_{0.8}\text{Ir}_{0.2})\text{O}_2:10\text{F}$ solid solution electrocatalysts possess higher roughness in comparison to that of bare Ti substrate and MnO_2 NRs, which predominantly offers a favorable structure for achieving facile intercalation of aqueous electrolyte on the electrode surface.⁹⁰ The improved wettability of $(\text{Mn}_{0.8}\text{Ir}_{0.2})\text{O}_2$ and $(\text{Mn}_{0.8}\text{Ir}_{0.2})\text{O}_2:10\text{F}$ electrodes would ensure the fast electrolyte penetration and accelerate oxygen release, thus offering enhancement in the OER kinetics.

3.2. Electrochemical Characterization of Electrocatalysts. Electrochemical impedance spectroscopy (EIS) analysis was carried out for the as-synthesized MnO_2 , $(\text{Mn}_{0.8}\text{Ir}_{0.2})\text{O}_2$, $(\text{Mn}_{0.8}\text{Ir}_{0.2})\text{O}_2:10\text{F}$, and IrO_2 electrocatalysts to investigate the charge transfer characteristics occurring on the as-prepared electrode surface. Figure 8a shows the EIS plots of $(\text{Mn}_{0.8}\text{Ir}_{0.2})\text{O}_2$, $(\text{Mn}_{0.8}\text{Ir}_{0.2})\text{O}_2:10\text{F}$, and IrO_2 (inset: EIS of MnO_2), obtained at ~ 1.45 V (vs RHE) in the electrolyte solution of 1 N H_2SO_4 at 40°C . Herein, as discussed in the Experimental Section, the semicircles in the Nyquist are plots (magnified EIS plots are depicted in Figure S6a, Supporting Information) of $(\text{Mn}_{0.8}\text{Ir}_{0.2})\text{O}_2$ and $(\text{Mn}_{0.8}\text{Ir}_{0.2})\text{O}_2:10\text{F}$ are fitted with $R_s(R_{ct}Q_{dl})-(R_{ct}Q_{dl})$ as an equivalent circuit model. As shown in Figure 8a and Table 2, the surface charge transfer resistance (R_{ct}), obtained from the diameter of the semicircle in the low-frequency region of the EIS (using the $R_s(R_{ct}Q_{dl})$ circuit model) plot of IrO_2 was obtained as $\sim 41 \Omega \text{ cm}^2$ while the solution resistance (R_s) was obtained as $\sim 12 \Omega \text{ cm}^2$, comparable to an earlier report.¹⁸ On the other hand, as expected, MnO_2 NRs exhibited a considerably higher R_{ct} ($>2200 \Omega \text{ cm}^2$) (inset of Figure 8a), which clearly reflects the poor electronic

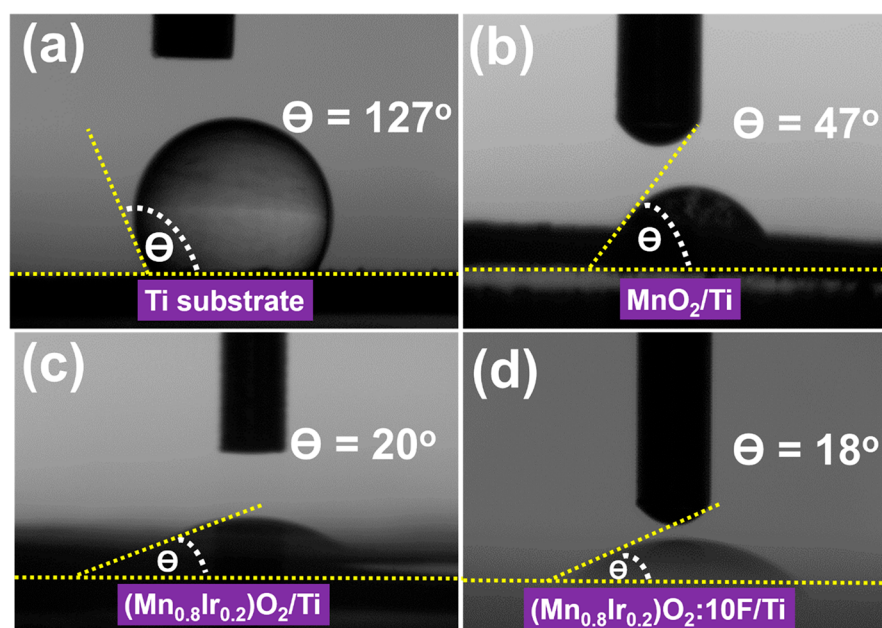


Figure 7. Contact angle images of (a) bare Ti substrate, (b) MnO_2 , (c) $(\text{Mn}_{0.8}\text{Ir}_{0.2})\text{O}_2$, and (d) $(\text{Mn}_{0.8}\text{Ir}_{0.2})\text{O}_2:10\text{F}$ NRs obtained from the droplet experiments.

conductivity and unfavorable electron transfer of MnO_2 NRs during the electrochemical catalytic processes.⁹¹

It is very interesting to note that $(\text{Mn}_{0.8}\text{Ir}_{0.2})\text{O}_2$ exhibits an R_c of $\sim 1.3 \Omega \text{ cm}^2$ and R_{ct} of $\sim 3.8 \Omega \text{ cm}^2$ —significantly lower than that of the as-synthesized pure IrO_2 as well as MnO_2 (Table 2). This result suggests the attainment of lower activation polarization and higher electronic conductivity after the introduction of minimal Ir content (20 atom %) into the parent MnO_2 framework. Similar results regarding reduction in the R_{ct} values of MnO_2 upon minimum Ir incorporation have been witnessed in the study conducted by Ye et al.⁵⁰ Additionally, as anticipated, the R_{ct} of $(\text{Mn}_{0.8}\text{Ir}_{0.2})\text{O}_2$ NRs was significantly further reduced after incorporation of 10 wt % F [$(\text{Mn}_{0.8}\text{Ir}_{0.2})\text{O}_2:10\text{F}$ NRs, $R_{ct} \approx 2.5 \Omega \text{ cm}^2$, $R_e \approx 0.7 \Omega \text{ cm}^2$]. Such impressive reduction in R_{ct} upon F doping evidently suggests an enhancement in the electronic conductivity of the parent MnO_2 material; thus, accordingly, $(\text{Mn}_{0.8}\text{Ir}_{0.2})\text{O}_2:10\text{F}$ is expected to have superior OER kinetics and electrochemical activity in comparison to pure IrO_2 and MnO_2 NRs as well as $(\text{Mn}_{0.8}\text{Ir}_{0.2})\text{O}_2$ NRs. These results are, hence, in excellent agreement with those discussed in Computational Study Results. Interestingly, it is also noteworthy to mention that the R_{ct} of the as-synthesized 1D $(\text{Mn}_{0.8}\text{Ir}_{0.2})\text{O}_2:10\text{F}$ NRs is ~ 1.6 -fold lower than that of our previously reported $(\text{Mn}_{0.8}\text{Ir}_{0.2})\text{O}_2:10\text{F}$ 2D thin film electrocatalyst ($R_{ct} \approx 4 \Omega \text{ cm}^2$).² This reduction in R_{ct} value is indeed contributed by the improved electronic charge transport: i.e., highly efficient facile charge (electron) transport pathways created on the entire $(\text{Mn}_{0.8}\text{Ir}_{0.2})\text{O}_2:10\text{F}$ 1D nanorod electrode by virtue of the nanorod morphology as well as between the electrocatalyst surface and the current collector (Ti substrate). Therefore, these experimental results collectively taken together indeed suggest that due to tailoring of the material's dimension (i.e., from 2D to 1D), the OER kinetics of $(\text{Mn}_{0.8}\text{Ir}_{0.2})\text{O}_2:10\text{F}$ electrocatalyst system was remarkably enhanced. Additionally, it is worth mentioning that the beneficial influence of F incorporation on reducing the R_{ct} values has also been demonstrated in the EIS results of fluorinated IrO_2 (Figure S6b) and MnO_2 (Figure S6c), wherein

$\text{IrO}_2:10\text{F}$ ($\sim 37 \Omega \text{ cm}^2$) and $\text{MnO}_2:10\text{F}$ ($\sim 2100 \Omega \text{ cm}^2$) exhibited R_{ct} lower than those of pristine IrO_2 and MnO_2 , respectively.

We next investigated the electrocatalytic OER activity of MnO_2 , $(\text{Mn}_{0.8}\text{Ir}_{0.2})\text{O}_2$, and $(\text{Mn}_{0.8}\text{Ir}_{0.2})\text{O}_2:10\text{F}$ electrocatalysts supported on a Ti substrate in 1 N H_2SO_4 at 40 °C and compared the performance with that of IrO_2 . Figure 8b depicts the iR_Ω corrected linear sweep voltammetry (LSV) curves for the as-prepared electrodes. As shown in Figure 8b and Table 2, the polarization curves of $(\text{Mn}_{0.8}\text{Ir}_{0.2})\text{O}_2$ NRs and $(\text{Mn}_{0.8}\text{Ir}_{0.2})\text{O}_2:10\text{F}$ NRs show an onset potential of ~ 1.35 V with respect to the RHE (reversible hydrogen electrode), which is similar to that of the $(\text{Mn}_{0.8}\text{Ir}_{0.2})\text{O}_2$ 2D thin film system as reported earlier.² This onset potential is, however, considerably lower (~ 80 mV) than that of IrO_2 (~ 1.43 V vs RHE), similar to earlier reports.^{16,18} On the other hand, MnO_2 NRs demonstrated extremely poor OER electrocatalytic activity with no sharp increase in current density (Figure 8b). Furthermore, to compare the apparent OER activity of these electrodes, the current density was measured at ~ 1.45 V vs RHE (typical potential considered to evaluate electrocatalytic performance of the electrocatalysts). As can be seen from Figure 8b and Table 2, $(\text{Mn}_{0.8}\text{Ir}_{0.2})\text{O}_2:10\text{F}$ NRs exhibit an excellent geometric current density of $\sim 12 \text{ mA cm}^{-2}_{\text{geo}}$, which is $\sim 600\%$, $\sim 218\%$, $\sim 220\%$, and $\sim 923\%$ higher than those of the in house synthesized IrO_2 ($\sim 2 \text{ mA cm}^{-2}_{\text{geo}}$), $(\text{Mn}_{0.8}\text{Ir}_{0.2})\text{O}_2$ NRs ($\sim 5.5 \text{ mA cm}^{-2}_{\text{geo}}$) and the previously reported 2D thin film architecture of $(\text{Mn}_{0.8}\text{Ir}_{0.2})\text{O}_2:10\text{F}$ ($\sim 5.45 \text{ mA cm}^{-2}_{\text{geo}}$)² and recently reported $\text{K}_{1.65}(\text{Mn}_{0.78}\text{Ir}_{0.22})_8\text{O}_{16}$ ($\sim 1.3 \text{ mA cm}^{-2}_{\text{geo}}$), respectively.⁴⁷ This remarkable increase in the current density of $(\text{Mn}_{0.8}\text{Ir}_{0.2})\text{O}_2:10\text{F}$ NRs is indeed credited to the enhanced charge transfer (i.e., lower R_{ct}) and formation of a unique electronic structure of F-incorporated $(\text{Mn}_{0.8}\text{Ir}_{0.2})\text{O}_2:10\text{F}$ NRs, as investigated by our theoretical calculations. However, as expected, MnO_2 NRs exhibited negligible OER activity ($\sim 0 \text{ mA cm}^{-2}_{\text{geo}}$, Figure 8b) in acid-assisted water electrolysis.^{92,93} This insignificant OER activity emerged from the significantly higher charge transfer resistance of MnO_2 NRs, indicating its poor electronic

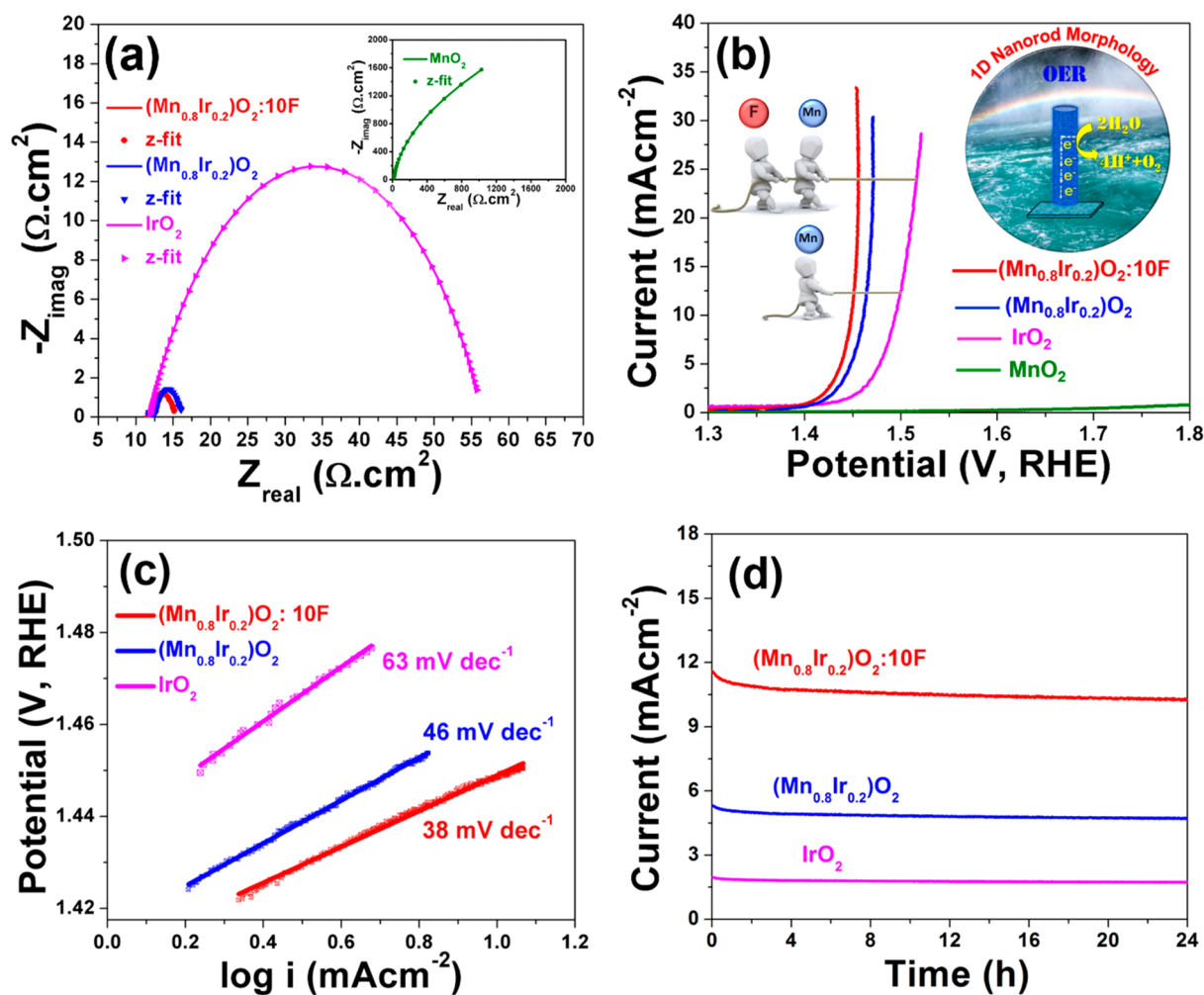


Figure 8. Comparison of electrochemical performances of the as-synthesized MnO_2 , $(\text{Mn}_{0.8}\text{Ir}_{0.2})\text{O}_2$, and $(\text{Mn}_{0.8}\text{Ir}_{0.2})\text{O}_2:10\text{F}$ NRs and the standard IrO_2 measured in a 1 N H_2SO_4 electrolyte at 40 °C: (a) EIS plots performed at ~ 1.45 V (vs RHE); (b) OER polarization (mA cm^{-2} vs potential) curves with a scan rate of 10 mV s^{-1} ; (c) Tafel plots of as-synthesized IrO_2 , $(\text{Mn}_{0.8}\text{Ir}_{0.2})\text{O}_2$, and $(\text{Mn}_{0.8}\text{Ir}_{0.2})\text{O}_2:10\text{F}$ NRs; (d) chronoamperometry (CA) tests conducted in 1 N H_2SO_4 solution under a constant potential of ~ 1.45 V (vs RHE) at 40 °C for 24 h.

Table 2. Results of Electrochemical Characterization for OER of As-Synthesized Electrocatalysts, Performed in 1 N H_2SO_4 Electrolyte Solution at 40 °C

electrocatalyst composition	onset potential (V vs RHE)	charge transfer resistance (R_{ct} , $\Omega \text{ cm}^2$)	current density at ~ 1.45 V ($\text{mA cm}^{-2}_{\text{geo}}$)	overpotential (η in mV) at $10 \text{ mA cm}^{-2}_{\text{geo}}$	Tafel slope (mV dec^{-1})	mass activity at ~ 1.45 V (A g^{-1})	ECSA ($\text{m}^2 \text{ g}^{-1}$)	TOF at ~ 1.45 V (s^{-1})
$(\text{Mn}_{0.8}\text{Ir}_{0.2})\text{O}_2$ NRs	~ 1.35	~ 3.8	~ 5.5	~ 240	46	~ 18.34	~ 419.04	~ 0.0054
$(\text{Mn}_{0.8}\text{Ir}_{0.2})\text{O}_2:10\text{F}$ NRs	~ 1.35	~ 2.5	~ 12	~ 200	38	~ 40	~ 704.76	~ 0.010
IrO_2	~ 1.43	~ 41	~ 2	~ 280	63	~ 6.67	~ 214.28	~ 0.0038
MnO_2 NRs	~ 1.8	~ 2300	~ 0		300			

conductivity/kinetics toward the acidic OER. In addition, it can be seen from Table 2 that, $(\text{Mn}_{0.8}\text{Ir}_{0.2})\text{O}_2:10\text{F}$ NRs delivered benchmark current densities of 10 and 20 mA cm^{-2} at overpotentials of ~ 200 and ~ 238 mV (with respect to the equilibrium OER potential, 1.23 V vs RHE), respectively, clearly outperforming IrO_2 , $(\text{Mn}_{0.8}\text{Ir}_{0.2})\text{O}_2$ NRs, and thin film of $(\text{Mn}_{0.8}\text{Ir}_{0.2})\text{O}_2:10\text{F}$,² which required overpotentials of ~ 280 , ~ 240 , and 245 mV to reach a current density of 10 mA cm^{-2} . Furthermore, in accordance with the EIS results, F-incorporated $\text{IrO}_2:10\text{F}$ (Figure S6d, Supporting Information) and $\text{MnO}_2:10\text{F}$ (Figure S6e) displayed higher OER catalytic activity, which evidently suggests the beneficial impact of F on the current

density. Herein, it is worth mentioning that our as-prepared 1D $(\text{Mn}_{0.8}\text{Ir}_{0.2})\text{O}_2:10\text{F}$ NRs demonstrated substantially lower overpotential (~ 200 mV) in comparison to various other reported electrocatalysts for the acidic OER, including the recently reported Ir-doped cryptomelane-type manganese oxide $[\text{K}_{1.65}(\text{Mn}_{0.78}\text{Ir}_{0.22})_8\text{O}_{16}]^{47}$ (~ 340 mV), illustrating the superior electrocatalytic performance of $(\text{Mn}_{0.8}\text{Ir}_{0.2})\text{O}_2:10\text{F}$ NRs toward water splitting. Thus, the improved OER activity of the $(\text{Mn},\text{Ir})\text{O}_2$ system evidently stems from the synergistic effect of IrO_2 and α -/ β - MnO_2 crystal structures. The obtained results are indeed in good agreement with the earlier work on an Ir-Mn oxide film system for the acidic OER, wherein the mixed $\text{IrO}_2(x)$

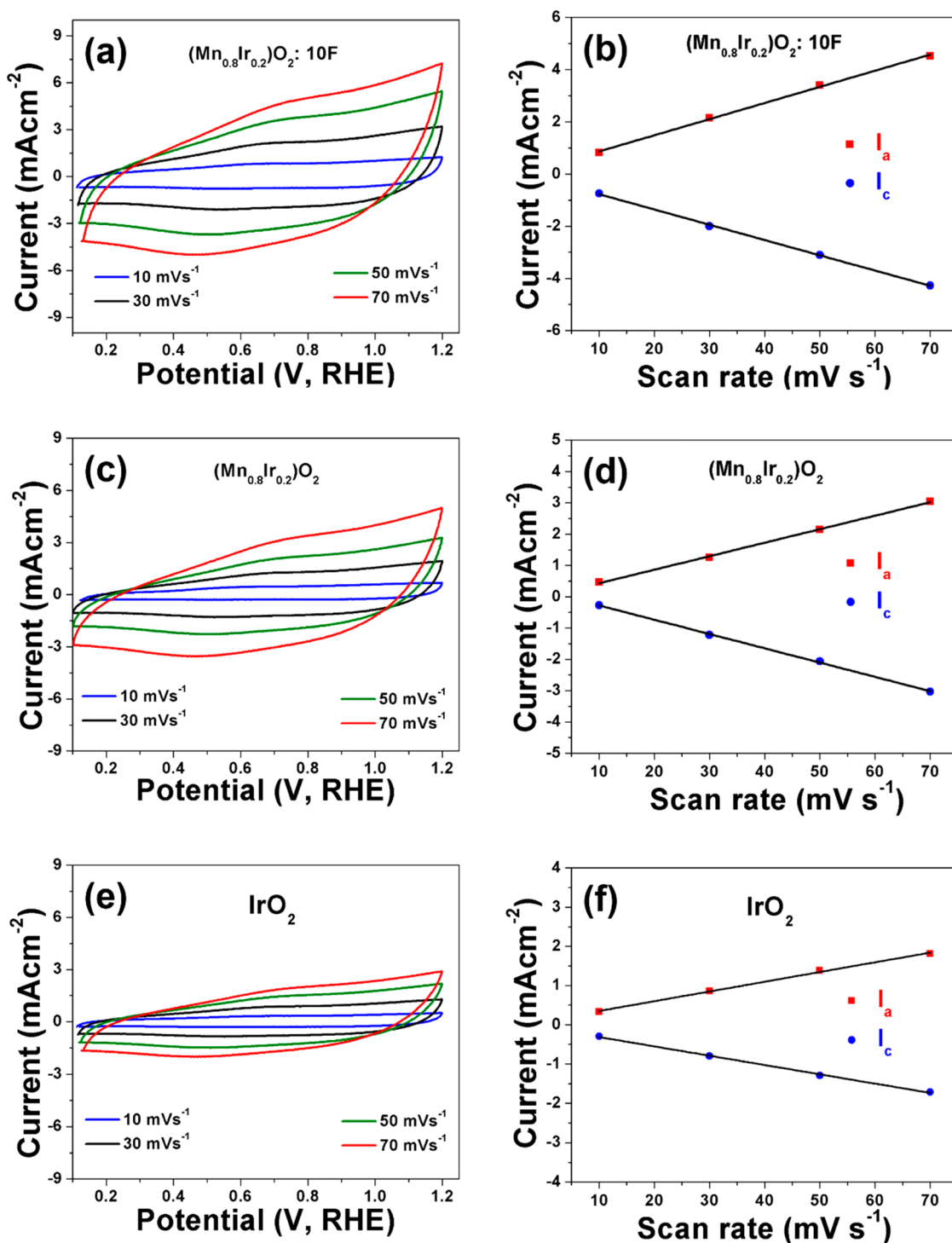


Figure 9. Cyclic voltammograms and the capacitive currents at 0.70 V vs RHE with scan rates of 10, 30, 50, and 70 mV s^{-1} in 1 N H_2SO_4 solution for as-synthesized (a, b) $(\text{Mn}_{0.8}\text{Ir}_{0.2})\text{O}_2\text{:}10\text{F}$ NRs, (c, d) $(\text{Mn}_{0.8}\text{Ir}_{0.2})\text{O}_2$ NRs, and (e, f) IrO_2 electrocatalysts.

+ $\text{MnO}_2(1-x)$ revealed electrocatalytic performance superior to that of the pristine rutile IrO_2 and $\beta\text{-MnO}_2$.⁵⁰ Furthermore, it is worth pointing out that our previously reported 2D thin film of $(\text{Mn}_{0.8}\text{Ir}_{0.2})\text{O}_2\text{:}10\text{F}$ was directly fabricated on the Ti substrate (i.e., without utilizing Nafion binder), whereas in the current work, Nafion 117 (5 wt % solution in lower aliphatic alcohols) binder was used for the preparation of the electrocatalyst inks. Therefore, the contribution of Nafion to the electrochemical activity needs to be verified and discussed. Accordingly, we prepared Nafion-containing electrodes (mass loading ~ 0.3 mg

cm^{-2}) and the electrochemical characterizations (impedance and polarization) were performed under OER conditions similar to those of other as-synthesized electrocatalyst materials studied in the current work. It can be clearly seen from Figure S6f,g that a Nafion-coated working electrode possesses negligible catalytic activity for the acidic OER, which is ably complemented by its very high charge transfer resistance ($>5000 \Omega \text{ cm}^2$), clearly suggesting its negligible OER performance. Thus, these results markedly indicate the insignificant contribution of Nafion

toward the observed reduction in the R_{ct} of 1D $(\text{Mn}_{0.8}\text{Ir}_{0.2})\text{O}_2$:10F as well as to the measured OER electrochemical activity.

Herein, although 1D $(\text{Mn}_{0.8}\text{Ir}_{0.2})\text{O}_2$:10F NRs demonstrate electrocatalytic activity superior to that of other as-synthesized electrocatalysts, evaluation of the intrinsic OER activity of these catalyst materials is very essential to draw conclusions about the increased OER activity of $(\text{Mn}_{0.8}\text{Ir}_{0.2})\text{O}_2$:10F NRs as perceived from the polarization curves (Figure 8b). Therefore, normalization of the current density by the BET surface area and calculations of the electrochemical active surface area (ECSA) and mass loading as well as calculations of the turnover frequency (TOF) have been carried out (see the Supporting Information for calculation details). The calculated corresponding mass activity, BET normalized current density ($\text{mA cm}^{-2}_{\text{BET}}$), ECSA normalized current density ($\text{mA cm}^{-2}_{\text{ECSA}}$), and TOF of $(\text{Mn}_{0.8}\text{Ir}_{0.2})\text{O}_2$:10F NRs was found to be $\sim 40 \text{ A g}^{-1}$, $1.126 \text{ mA cm}^{-2}_{\text{BET}}$, $5.6 \mu\text{A cm}^{-2}_{\text{ECSA}}$, and 0.01 s^{-1} , respectively, at an overpotential of 220 mV (see the Supporting Information for calculation details). All of these values are demonstratively higher than those of IrO_2 , $(\text{Mn}_{0.8}\text{Ir}_{0.2})\text{O}_2$ NRs, and the previously reported $(\text{Mn}_{0.8}\text{Ir}_{0.2})\text{O}_2$:10F thin film electrocatalyst, evidently revealing the superior intrinsic OER electrocatalytic activity of $(\text{Mn}_{0.8}\text{Ir}_{0.2})\text{O}_2$:10F NRs. This excellent activity of $(\text{Mn}_{0.8}\text{Ir}_{0.2})\text{O}_2$:10F NRs is a characteristic indicator of the enhancement in the OER kinetics, i.e. lower R_{ct} (i.e., efficient electron transport along the 1D NRs), as well as the beneficial electronic structure modification achieved upon F-substituted solid solution formation, which has been expertly supported by our DFT calculations (Computational Study Results). Next, the lower Tafel slope of $(\text{Mn}_{0.8}\text{Ir}_{0.2})\text{O}_2$:10F NRs ($\sim 38 \text{ mV dec}^{-1}$) (Figure 8c and Table 2) in comparison to those of $(\text{Mn}_{0.8}\text{Ir}_{0.2})\text{O}_2$ ($\sim 46 \text{ mV dec}^{-1}$), IrO_2 ($\sim 63 \text{ mV dec}^{-1}$),^{94–96} and the recently reported⁴⁷ $\text{K}_{1.65}(\text{Mn}_{0.78}\text{Ir}_{0.22})_8\text{O}_{16}$ ($\sim 76 \text{ mV dec}^{-1}$) suggests the favorable OER kinetics with faster electron transport and enhanced electrical conductivity/electrocatalytic activity. The significantly higher Tafel slope for MnO_2 ($\sim 300 \text{ mV dec}^{-1}$) (Table 2, Figure S7a) indicates its inferior OER kinetics toward water splitting under acidic conditions.

In addition to the excellent electrocatalytic activity, long-term electrochemical stability is indeed an important criterion for assessing the high-performance of OER electrocatalysts. Thus, to investigate the endurance of the as-synthesized electrocatalysts for the OER in 1 N H_2SO_4 electrolyte media, chronoamperometry (CA) tests at a constant potential of 1.45 V (vs. RHE) in 1 N H_2SO_4 at 40 °C for 24 h were carried out. As depicted in Figure 8d, the as-synthesized $(\text{Mn}_{0.8}\text{Ir}_{0.2})\text{O}_2$:10F electrocatalyst demonstrated excellent long-lasting durability over 24 h, comparable to that of $(\text{Mn}_{0.8}\text{Ir}_{0.2})\text{O}_2$ NRs, IrO_2 , and the thin film of $(\text{Mn}_{0.8}\text{Ir}_{0.2})\text{O}_2$:10F. Furthermore, to bolster these results of excellent electrochemical stability, we conducted elemental analyses using inductively coupled plasma-optical emission spectroscopy (ICP-OES) to determine the amount of Mn and/or Ir that might have leached out from the electrode surface into the electrolyte solution. The ICP-OES analysis revealed negligible dissolution of Mn and Ir from the as-prepared $(\text{Mn}_{0.8}\text{Ir}_{0.2})\text{O}_2$:10F, $(\text{Mn}_{0.8}\text{Ir}_{0.2})\text{O}_2$, and IrO_2 electrocatalysts, suggesting the remarkable structural stability of these as-synthesized electrocatalysts (Table S6). In addition, an ICP-OES analysis performed on the electrodes post-stability tests showed Mn:Ir ratios as 80.32:19.68 and 79.91:20.09 for $(\text{Mn}_{0.8}\text{Ir}_{0.2})\text{O}_2$:10F and $(\text{Mn}_{0.8}\text{Ir}_{0.2})\text{O}_2$, respectively, which are in a good agreement with the poststability EDX results discussed in the Supporting Information. On the other hand, MnO_2

displayed extremely poor electrochemical OER stability with a rapid drop in current density (Figure S7b), similar to the earlier studies of MnO_2 as an OER electrocatalyst.^{91,92} Thus, it is interesting to note that the incorporation of reduced amounts of IrO_2 into the framework structure of MnO_2 along with incorporation of F not only significantly improved the OER kinetics but also enhanced the electrochemical stability of pure MnO_2 NRs, as clearly evidenced from the chronoamperometry results. The stabilizing effect of F on the transition metal oxide (TMO) based supports has been comprehensively investigated by various groups. For example, Geiger et al.⁵¹ investigated the influence of various dopants (fluorine, indium, antimony) incorporated in transition metal oxides such as SnO_2 . On the basis of the potential-dependent dissolution rates of these oxides, Geiger et al. concluded that fluorine-doped tin oxide (FTO) shows the best OER stability in 0.1 M H_2SO_4 electrolyte with a stability window of FTO ranging from $-0.34 \text{ V RHE} < E < 2.7 \text{ V RHE}$ with no indication of any measurable dissolution for compositions between these limits, making fluorine a promising dopant for the acidic OER conditions among indium tin oxide (ITO) and antimony-doped tin oxide (ATO) based supports. In addition, in a theoretical study conducted by Binniger et al.,⁹⁷ it has been reported that oxygen anion free salts containing anion species with a very high oxidation potential such as fluorides, chlorides, and sulfates are indeed promising candidates as well as truly thermodynamically stable OER catalysts. Therefore, in the present study, F doping not only enhances the electronic conductivity of MnO_2 but also is beneficial for stabilizing the as-synthesized electrocatalysts crystal structure and morphology for the acidic OER.

Furthermore, we evaluated the electrochemically active surface area (ECSA) to gain deeper insights into the OER electrocatalytic activity. Herein, in order to determine the ECSA of $(\text{Mn}_{0.8}\text{Ir}_{0.2})\text{O}_2$ NRs, $(\text{Mn}_{0.8}\text{Ir}_{0.2})\text{O}_2$:10F NRs, and IrO_2 electrocatalysts, the electrical double-layer capacitance (EDLC) measurements were carried out in 1 N H_2SO_4 electrolyte at 40 °C. Figure 9a,c,e shows the cyclic voltammogram (CV) curves recorded at various scan rates (10, 30, 50, and 70 mV s^{-1}). It can be clearly seen in Figure 9b that $(\text{Mn}_{0.8}\text{Ir}_{0.2})\text{O}_2$:10F NRs exhibited anodic (j_a) and cathodic (j_c) current densities relatively higher than those of $(\text{Mn}_{0.8}\text{Ir}_{0.2})\text{O}_2$ and IrO_2 (Figure 9d,f, respectively). Next, the double-layer capacitance (C_{dl}) was determined from the linear slope of the current density ($j_a - j_c$) vs scan rate (which is equivalent to twice the double-layer capacitance, C_{dl}), following previous studies for ECSA calculations (see the Supporting Information for calculation details).^{98,99} The considerably higher C_{dl} ($\sim 74 \text{ mF cm}^{-2}$) of $(\text{Mn}_{0.8}\text{Ir}_{0.2})\text{O}_2$:10F NRs indicates that it possesses a greater catalytically active surface than $(\text{Mn}_{0.8}\text{Ir}_{0.2})\text{O}_2$ ($\sim 44 \text{ mF cm}^{-2}$) and IrO_2 ($\sim 22.5 \text{ mF cm}^{-2}$). Furthermore, the ECSA ($\text{m}^2 \text{ g}^{-1}$) of the as-synthesized electrocatalysts was obtained by dividing double-layer capacitance (C_{dl}) by the specific capacitance (C^*) of the electrocatalyst, similar to the previous reports of ECSA determination.^{100–102} A general specific capacitance (C^*) of metal electrodes in acidic solutions is taken as $35 \mu\text{F cm}^{-2}$.^{100,103,104} On the basis of this specific capacitance ($C^* \approx 35 \mu\text{F cm}^{-2}$) value, the ECSA of $(\text{Mn}_{0.8}\text{Ir}_{0.2})\text{O}_2$:10F NRs was obtained as $\sim 704.76 \text{ m}^2 \text{ g}^{-1}$, which is remarkably higher than those of $(\text{Mn}_{0.8}\text{Ir}_{0.2})\text{O}_2$ NRs ($\sim 419.04 \text{ m}^2 \text{ g}^{-1}$), IrO_2 ($\sim 214.28 \text{ m}^2 \text{ g}^{-1}$), and Ir-doped cryptomelane-type manganese oxide ($\sim 55 \text{ m}^2 \text{ g}^{-1}$) as reported in a recent study⁴⁷ (see the Supporting Information for the detailed ECSA analysis). As elucidated in the Introduction,

owing to the large aspect ratio (L/D) and high density of active sites, 1D nanomaterials commonly exhibit superior electrochemically active surface areas. For example, in the study conducted by Wang et al., a 1D Pd/Pt NW array demonstrated an extremely high electrochemical active area of $\sim 6791 \text{ m}^2 \text{ g}^{-1}$, which is ~ 51 -fold higher than that of a thin film architecture of Pt ($\sim 133 \text{ m}^2 \text{ g}^{-1}$).¹⁰⁵ Such excellent electrochemically active surface area materials can show markedly improved electrocatalytic activity, offering efficient catalyst utilization for electrochemical processes.¹⁰⁶ Furthermore, the higher roughness factor (RF) for $(\text{Mn}_{0.8}\text{Ir}_{0.2})\text{O}_2:10\text{F}$ NRs (~ 2114.28) in comparison to those of $(\text{Mn}_{0.8}\text{Ir}_{0.2})\text{O}_2$ NRs (~ 1257.14) and IrO_2 (~ 642.85) clearly indicates the enhancement of the real electrochemical surface area (Table S4a) in comparison with the geometric area of the electrode (see the Supporting Information for calculation details). Moreover, the above results are in excellent agreement with the contact angle analysis (Figure 7), wherein $(\text{Mn}_{0.8}\text{Ir}_{0.2})\text{O}_2:10\text{F}$ NRs (~ 2114.28) exhibited a relatively lower water contact angle: i.e., higher roughness factor. In addition, in the present study, ECSA has also been evaluated by utilizing the specific capacitance (C^*) of single-crystal IrO_2 ($\sim 650 \mu\text{F cm}^{-2}$)^{3,102} (see Table S4b, Supporting Information, for more details on the discrepancy in ECSA results). Values obtained using the C^* for single-crystal IrO_2 , though lower, nevertheless still indicate that the F-doped compositions of $(\text{Mn}_{0.8}\text{Ir}_{0.2})\text{O}_2:10\text{F}$ reflect higher ECSA values in comparison to the undoped $(\text{Mn}_{0.8}\text{Ir}_{0.2})\text{O}_2$ and IrO_2 , in agreement with the arguments presented above.

It is worth mentioning that although $(\text{Mn}_{0.8}\text{Ir}_{0.2})\text{O}_2:10\text{F}$ NRs exhibited a lower BET specific area ($\sim 3.55 \text{ m}^2 \text{ g}^{-1}$) in comparison to those of $(\text{Mn}_{0.8}\text{Ir}_{0.2})\text{O}_2$ and IrO_2 (Table 1 and Figure 3), the ECSA measurements revealed that 1D $(\text{Mn}_{0.8}\text{Ir}_{0.2})\text{O}_2:10\text{F}$ NRs possess an intrinsically higher electrocatalytically “active” surface area ($\sim 704.76 \text{ m}^2 \text{ g}^{-1}$), enabling more active sites to be exposed to the electrolyte, which in principle contributed to the enhanced OER kinetics. Such a general discrepancy in area obtained by BET and ECSA is well elucidated in a recent study conducted by Jung et al.¹⁰³ According to this study, BET is an empirical technique to determine the “total” surface area which can over- or underestimate the true catalytically “active” surface area. Thus, it is recommended to normalize the current density by BET as well as ECSA, which can essentially provide a conservative estimate of the specific activity of the electrocatalysts. Hence, accordingly the obtained current densities from LSV curves (Figure 8b) were normalized to the BET as well as ECSA area values. It can be seen from Table S5 that, 1D $(\text{Mn}_{0.8}\text{Ir}_{0.2})\text{O}_2:10\text{F}$ NRs still demonstrated higher BET and ECSA specific activity in comparison to those of $(\text{Mn}_{0.8}\text{Ir}_{0.2})\text{O}_2$ and IrO_2 . This clearly accentuates the intrinsically superior OER electrocatalytic activity of 1D $(\text{Mn}_{0.8}\text{Ir}_{0.2})\text{O}_2:10\text{F}$ NRs, proffered by the lower charge transfer resistance (i.e., lower activation polarization) and unique F-containing solid solution formation as discussed in detail in the Computational Study Results.

Finally, in order to investigate the structural stability and mechanical integrity of the high-performance $(\text{Mn}_{0.8}\text{Ir}_{0.2})\text{O}_2:10\text{F}$ NRs electrocatalyst after its rigorous OER stability test conducted in harsh acidic medium, characterizations (XRD, SEM, XPS) following post-stability tests were carried out. As shown in Figure S8, post-XRD patterns collected on $(\text{Mn}_{0.8}\text{Ir}_{0.2})\text{O}_2:10\text{F}$ did not feature any major changes in the XRD peak positions, suggesting that the $(\text{Mn}_{0.8}\text{Ir}_{0.2})\text{O}_2:10\text{F}$ structure is well maintained, retaining its original tetragonal

phase with no undesired crystal phase transformations. In addition, the electrocatalysts following poststability chronoamperometry tests were subjected to SEM analyses. Accordingly, SEM images (Figure S9a,b) and EDX spectrum (Figure S9c) collected on $(\text{Mn}_{0.8}\text{Ir}_{0.2})\text{O}_2:10\text{F}/\text{Ti}$ revealed the existence of 1D nanorod architectures similar to those shown in Figure 4, indicating no significant change or deterioration of the morphology of the electrocatalyst as well as no change in the elemental composition following the electrochemical stability test. These results thus not only indicate the robust nature of the electrocatalysts but also suggest the firm adhesion/binding of $(\text{Mn}_{0.8}\text{Ir}_{0.2})\text{O}_2:10\text{F}$ NRs on the current collector substrate. Furthermore, post-XPS characterizations (Figure S10) revealed the stable state of the $(\text{Mn}_{0.8}\text{Ir}_{0.2})\text{O}_2:10\text{F}$ electrode indicating the presence of Mn, Ir, and O. Furthermore, the XPS spectrum of Mn (Figure S10a) indicated a negative shift in the XPS peak positions after a 24 h durability test in comparison with the pristine $(\text{Mn}_{0.8}\text{Ir}_{0.2})\text{O}_2:10\text{F}$ NRs. Such lower binding energy shifts in the case of Mn 2p peak position indicate an electronic environment change during the OER (suggesting manganese(III) oxyhydroxide (MnOOH) formation).^{107–109} Such beneficial surface modification (i.e., formation of metastable OER-active Mn^{3+} ions^{107,109}) during the prolonged exposure to the OER conditions is commonly observed in various electrocatalyst materials, which plays a critical role in stimulating the OER kinetics as well as shielding both the dissolution and disproportionation of MnO_2 under the harsh acidic OER conditions.^{108,109} Interestingly, in the XPS spectrum of Ir (Figure S10b) of $(\text{Mn}_{0.8}\text{Ir}_{0.2})\text{O}_2:10\text{F}$ NRs following the stability tests, Ir $4f_{5/2}$ and Ir $4f_{7/2}$ doublet positions also exhibited a negative shift of $\sim 0.25 \text{ eV}$ in comparison to the freshly prepared $(\text{Mn}_{0.8}\text{Ir}_{0.2})\text{O}_2:10\text{F}$. Such negative shifts in the doublet positions of an Ir-containing electrocatalyst were similarly detected in earlier studies conducted by Siracusano et al.⁵² and Ghadge et al.,³ which indicates the formation of substoichiometric IrO_x , i.e. partial conversion of IrO_2 to the hydrated substoichiometric IrO_x species, during prolonged exposure to the OER conditions. For example, as elucidated by Huang et al.,¹¹⁰ in the XPS spectrum of poststability $(\text{Mn}_{0.8}\text{Ir}_{0.2})\text{O}_2:10\text{F}$ (Figure S10b), in addition to the peak at $\sim 62 \text{ eV}$ (Ir^{4+}), other peaks at ~ 62.9 and 67 eV were observed which correspond to those of Ir^{3+} and Ir^{6+} , respectively.¹¹⁰ According to various literature reports,^{52,110} the shifts in the binding energy as well as the formation of different oxidation states of Ir^{n+} can be attributed to the presence of lattice oxidized ion O^{2-} or hydroxide or bound water/adsorbed H_2O or O_2 on the surface. Such surface modification developing during the intense rate of oxygen evolution is considered to be beneficial, resulting in enhancement in the OER kinetics.⁵² In the comprehensive XPS study conducted by Siracusano et al.,⁵² the formation of hydrated substoichiometric species and the positive influence of weakly bonded surface hydroxyls in Ir-based electrocatalysts on the OER catalytic activity have been exclusively elucidated. In addition, from various studies it has been identified that the surface OH groups play a crucial role as reactive surface intermediates on the active sites of the oxygen evolution process. Thus, in accordance with the above discussions, as witnessed in our poststability XPS characterizations, the modified electronic environments of Ir and Mn evidently suggest the acceleration of OER kinetics.

In line with the above discussion, the XPS spectrum of O (Figure S10c) shows, in addition to a peak at $\sim 530.8 \text{ eV}$, two more peaks. The peak at $\sim 533 \text{ eV}$ can be ascribed to a low binding energy component (LBEC) which is attributed to the

enhanced hydroxide formation¹¹⁰ during the OER, similar to the case for the earlier reported studies.^{52,71,111} In the recent Copoed IrCu OER electrocatalyst work by Kwon et al.,¹¹² such an increase in the peak intensity (at a binding energy of ~ 533 eV) is ascribed to the evolution of IrO_x species as well as surface Ir–OH species. As mentioned above as well as in good agreement with various reported studies,^{112–114} the formation of an Ir(O)_x(OH)_y phase is regarded as an active phase for the OER. Thus, these post mortem XPS characterizations results suggest the beneficial surface modification of Ir and Mn during the OER process. The peak observed at a higher binding energy value of ~ 536 eV corresponds to Nafion,¹¹⁵ which is used as a binder during the preparation of the electrocatalyst ink (discussed in [Experimental Methodology](#)). Herein it is important to underline that, the primary objective of the present work is to demonstrate the promising attributes of 1D architectures. Although our preliminary XPS results indicate the beneficial surface amendment and change in the electronic environment of the as-synthesized (Mn_{0.8}Ir_{0.2})O₂:10F system during extended OER, an in-depth poststability structural analysis (computational as well as experimental) is highly desirable to advance the understanding of the structural parameters and surface modifications occurring during the OER process that can contribute to the high OER activity and electrochemical durability ([Figure S11](#)). Such fundamental electrochemical benchmarking studies will be the object of our successive work on the Ir-based OER electrocatalyst systems for acid-mediated water electrolysis.

3.3. Computational Study Results. **3.3.1. Computational Study of the Electrochemically Active α -MnO₂ Based Electrocatalysts.** The main origins of the enhanced electrocatalytic activity of fluorine-doped Mn_{0.75}Ir_{0.25}O₂ could be understood from an electronic structure point of view as well as from a thermodynamic consideration of all the four elementary steps of the OER occurring at the active surface of the electrocatalyst. Similar to our previous publications,^{2,16,18} we have continued to adopt the concept proposed by Nørskov and his group,^{54,116} and accordingly, we have used it for qualitative evaluation of the electrochemical activity of Mn_{0.75}Ir_{0.25}O₂ and Mn_{0.75}Ir_{0.25}O₂:F electrocatalysts. As mentioned earlier in [Computational Methodology](#), the electronic structures of the stable surfaces for all the electrocatalysts have been calculated and the positions of the corresponding d band centers have been obtained as a first moment of $n_d(E)$: $\varepsilon_d = \int n_d(E)E dE / \int n_d(E) dE$, where $n_d(E)$ is the projected d band density of states of the corresponding materials. [Figure 10](#) thus accordingly depicts the projected d band densities of states together with the corresponding centers of these zones marked with vertical arrows on the graphs calculated for the (110) surface for pure α -MnO₂, Ir-substituted α -MnO₂, (Mn_{0.75}Ir_{0.25})O₂, and F-doped Ir-substituted α -MnO₂, (Mn_{0.75}Ir_{0.25})O_{1.75}F_{0.25}, (Mn_{0.75}Ir_{0.25})O_{1.375}F_{0.625}, and (Mn_{0.75}Ir_{0.25})O_{1.0}F_{1.0}. Since IrO₂ is a benchmark OER electrocatalyst, the d band positions for IrO₂, marked with a dashed vertical line throughout the whole graph, could serve as a reference point, showing the optimal electrocatalytic activity for the as-synthesized electrocatalysts.² In our previous studies^{2,16,18} we have showed that IrO₂ is characterized by d band centers located at ~ -1.33 eV marked with a solid vertical line at the graph. The closer the corresponding d band center position of the solid solution electrocatalyst studied herein is to -1.33 eV, the higher the electrocatalytic activity of the substituted solid solution will be expected to be, such that the d band center position can serve as

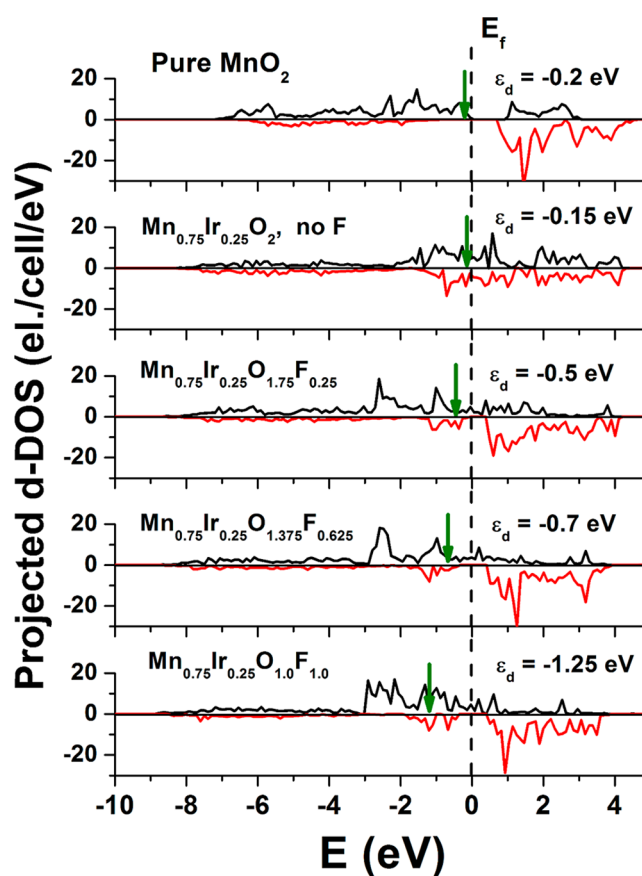


Figure 10. Projected d-band density of the electronic states calculated for pure α -MnO₂, (Mn_{0.75}Ir_{0.25})O₂, and F-doped (Mn_{0.75}Ir_{0.25})O₂ with 4, 10, and 15 wt % of F. The Fermi level is set to zero. The arrows denote the corresponding d band centers.

an indicator of the expected improvement in the overall electrocatalytic activity of the electrocatalyst. Such an approach can thus help in understanding the effect of fluorine on the electrocatalytic activity of α -(Mn, Ir)O₂:F.

It can be seen from [Figure 10](#) that MnO₂ is indeed a poor electronic conductor with a band gap of ~ 0.9 eV. Similar computations made by Tripkovic et al.¹¹⁷ indicated a corresponding value of 1.0 eV. The electronic conductivity ([Table S7](#), Supporting Information) of the as-synthesized MnO₂ at room temperature ($\sigma_{300\text{K}}$) was obtained as ~ 0.0032 S cm⁻¹ (resistivity, $\rho_{300\text{K}} \sim 312.5$ Ω cm), which is in good accordance with various literature reports.^{118,119} Thus, it can be inferred that such a structure of MnO₂ possessing substandard electronic conductivity would not be an efficient electrocatalyst for water splitting, which is indeed validated by the present impedance and polarization results. Also, the corresponding d band center of the material is located at -0.2 eV, which is far away from the optimal position of -1.33 eV featured by IrO₂, the benchmark electrocatalyst used for the OER in PEM-based electrolyzers. However, introduction of 20 atom % Ir into the α -MnO₂ lattice leads to lattice expansion ([Table S1](#)) and also improvement in the electronic conductivity ([Table S7](#)). The improved electronic conductivity of Ir-containing α -MnO₂ ((Mn_{0.8}Ir_{0.2})O₂) has been evidenced from the impedance as well as electrical conductivity measurements ($\sigma_{300\text{K}} = \sim 0.11$ S cm⁻¹). However, this modification of the electronic structure alone does not help improve the d band center position. It still locates the Fermi level in the vicinity of -0.15 eV of the energetic scale. Although an

improvement in the electronic conductivity would lead to an increase in the electrocatalytic activity of $(\text{Mn,Ir})\text{O}_2$ in comparison to that of pure MnO_2 , it still has the possibility to be further improved due to the suboptimal position of the d band center. Such improvement could be achieved with the introduction of fluorine into the $(\text{Mn,Ir})\text{O}_2$ lattice. Figure 10 clearly demonstrates the calculated projected density of d electronic states for $(\text{Mn,Ir})\text{O}_2$ with different F contents. One can see (Figure 10) that the addition of F from ~ 4 wt % up to ~ 15 wt % moves the d band center from -0.5 to -1.25 eV, which allows one to expect a significant improvement in the electrocatalytic activity. This shift in the d band center takes place due to the formation of the hybridized F 2p–Mn 3d and F 2p–Ir 5d electronic states well below the Fermi level. An identical effect of F on the electronic structure has also been seen earlier and reported by us in a similar study of $(\text{Sn,Ir})\text{O}_2$:F electrocatalysts.¹⁶ Similar to the case for $(\text{Mn,Ir})\text{O}_2$:F, the formation of F 2p–Ir 5d hybridized electronic states shifts the d band center of $(\text{Ir,Sn})\text{O}_2$:F down toward the optimal position and thus improves the overall electronic conductivity as well as the electrocatalytic activity of $(\text{Ir,Sn})\text{O}_2$:F with a substantial reduction of ~ 70 – 80% in the noble metal content.¹⁶ These theoretical findings have been well supported in the corresponding reports¹⁶ as well as in the experimental results of the present work wherein F-containing $(\text{Mn}_{0.8}\text{Ir}_{0.2})\text{O}_2$:10F exhibited improved electronic conductivity ($\sigma_{300\text{K}}$) of ~ 5.88 S cm^{-1} (Table S7).

Due to its simplicity, the d band center concept can provide only a qualitative explanation of the basic origins of the high electrocatalytic activity of $(\text{Mn,Ir})\text{O}_2$:F. In order to investigate the effects of Ir and F introduction into the α - MnO_2 lattice on the overpotential of the $(\text{Mn,Ir})\text{O}_2$:F solid solution oxide, there is a need to consider all the four elementary steps involved in the oxygen evolution reaction, as outlined in Computational Methodology (eq 1). Figure 11a demonstrates the free energies of all the four elementary steps of the OER calculated for pure α - MnO_2 and the three different atomic configurations with introduction of Ir and F atoms discussed above and illustrated in Figure 1b–d. Also, some of the data used for plotting these graphs have been collected in Table 3. It can be seen that the most energetically challenging step for all the four systems is step III, which results in the formation of the hydroperoxide HOO^* from the second water molecule. This step determines the major overpotential required to overcome in order to meet the four steps of OER outlined in Figure 11a,b. For pure α - MnO_2 the OER overpotential is $1.41 - 1.23 = 0.18$ V (Figure 11a), while for $(\text{Mn,Ir})\text{O}_2$ it is 0.20 and 0.23 V for the two different positions of Mn and Ir in the unit cell. Thus, these results indicate that the presence of Ir in MnO_2 increases the overpotential for the OER in comparison with that of pure MnO_2 . Such an increase in the energy difference for the third elementary step in the case of Ir-doped MnO_2 is attributable to the weaker interaction between the adsorbed oxygen (O^*) and the surface, resulting in an increase in the total energy of the system in comparison with pure MnO_2 , making it less feasible for the species to adsorb at the surface and thus, resulting in an increase in the overpotential of the overall OER for the $(\text{Mn,Ir})\text{O}_2$ electrocatalyst system. Furthermore, it can be seen from Figure 11a that the additional introduction of F into the $(\text{Mn,Ir})\text{O}_2$ oxide system leads to a slight reduction in the overpotential from 0.20 to 0.19 V, evidently suggesting a reduced reaction barrier and improved electrocatalytic activity in comparison to that of undoped $(\text{Mn,Ir})\text{O}_2$ oxide. From these results one can conclude that,

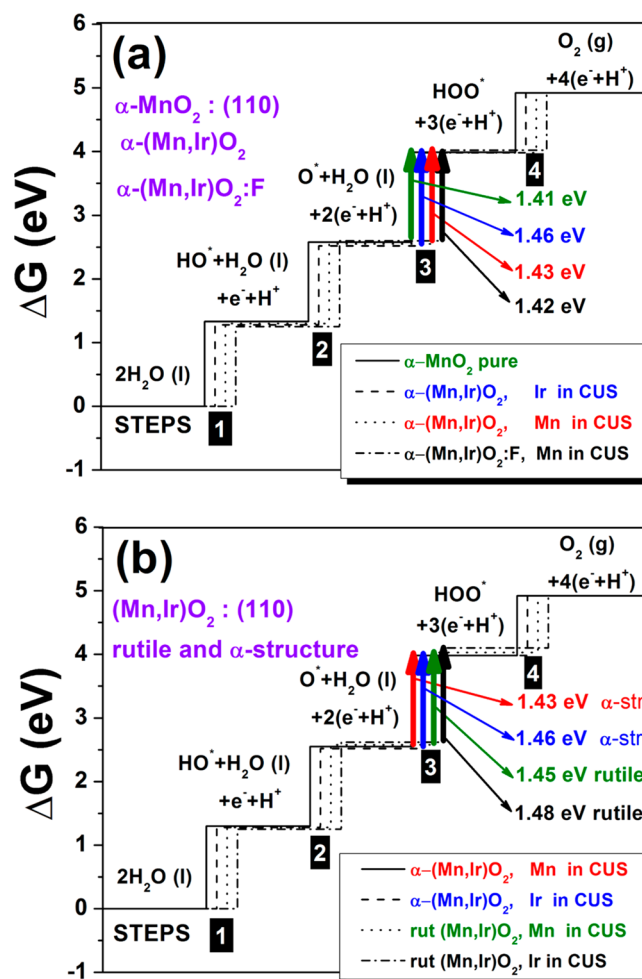


Figure 11. Free energies of the intermediate reactions for (a) pure and Ir-doped α - MnO_2 with the same CUS at (110) surfaces and (b) Ir-doped α - MnO_2 and Ir-doped rutile MnO_2 with the same CUS at (110) surfaces.

among all the materials considered in the present study (i.e., pure MnO_2 and MnO_2 doped with Ir and F), pure MnO_2 is expected to have the lowest overpotential for the OER reaction. This result indicates that the MnO_2 electrocatalyst itself intrinsically has a good ability to oxidize water very efficiently, provided it attains good electronic conductivity together with excellent electrochemical stability under the harsh acidic OER conditions of PEM water electrolysis. Both of these properties related to electrocatalytic activity as well as electrochemical stability are fairly mediocre in α - MnO_2 (owing to its semiconducting nature and poor OER stability in the acidic environment), which together suggest that there is a strong need to improve the electronic conductivity and electrochemical stability by introduction of some appropriate elements into the MnO_2 framework. In this direction, the approach of incorporating active/foreign elements into the earth-abundant and cheap materials has been widely employed to fabricate high-performance electrocatalyst systems (Table S8). Such elements, though tend to be noble metals (Ir, Ru, Pt) although not desirable, could modify the electronic structure and the overall structural stability in a positive manner, allowing one to synthesize highly efficient and completely noble metal free electrocatalyst systems for the acid-assisted oxygen evolution reaction. Along these lines, it is worth mentioning that various

Table 3. Computational Data Obtained from the Present Study. (^a)

configuration	$\Delta ZPE - T\Delta S$ (eV)	ΔG (eV)					
		pure α -MnO ₂	α -(Mn,Ir)O ₂ Ir at Pos.1	α -(Mn,Ir)O ₂ Ir at Pos.2	α -(Mn,Ir)O ₂ :F Ir at Pos.2	rutile (Mn,Ir)O ₂ Ir at Pos.1	rutile (Mn,Ir)O ₂ Ir at Pos.2
Vac + 2H ₂ O		0	0	0	0	0	0
HO* + H ₂ O + 1/2H ₂	0.35	1.33	1.28	1.30	1.25	1.25	1.28
O* + H ₂ O + H ₂	0.05	2.58	2.52	2.55	2.60	2.62	2.58
HOO* + 3/2H ₂	0.40	3.99	3.98	3.98	4.02	4.10	4.03
vac + O ₂ + 2H ₂		4.92	4.92	4.92	4.92	4.92	4.92
ΔG of step III (eV) (overpotential in V)		1.41 (0.18)	1.46 (0.23)	1.43 (0.20)	1.42 (0.19)	1.48 (0.25)	1.45 (0.22)

^a $\Delta ZPE - T\Delta S$ data were taken from a previously published study.⁵³

researchers have already embarked on a journey to explore various acid stable element doped MnO₂ electrocatalyst systems for the acidic OER (for example, recent work on the Mn_{0.8}Ti_{0.2}O₂ electrocatalyst system reported by Frydendal et al.,¹²⁰ the (Mn-Co-Ta-Sb)O_x system reported by Shinde et al.,¹²¹ the Ni_xMn_{1-x}Sb_{1.6-1.8}O_y electrocatalyst by Moreno-Hernandez,¹²² CoMnO_x work by Nocera and co-workers,^{123,124} etc.).

Furthermore, another aspect of the present study is to compare the catalytic activity of 1D α -(Mn,Ir)O₂ NRs with that of a 2D thin film (Mn,Ir)O₂ system having a rutile crystal structure, as reported by us recently.² Figure 11b depicts the free energies of all the four intermediate steps of the OER reaction for both rutile and the α structures of (Mn,Ir)O₂. Graphs for the two Ir-Mn configurations with a rutile structure are taken from an earlier report,² while another two graphs reflect the calculated free energies for the α structure and are reproduced from Figure 11a for the α -(Mn,Ir)O₂ system. It can be seen that, for both atomic configurations at (110), the rate-determining step (steps III) for the α structure demonstrate consistently lower values than the corresponding step III for the (110) rutile structure (Figure 11b). The lowest free energy for step III is 1.43 eV for the α structure with Mn atom under the CUS. The corresponding value for step III at the rutile surface is 1.45 eV with a similar atomic configuration. The difference in the overpotential for the same CUS but with different local distribution of the Mn and Ir ions is ~ 0.02 – 0.03 eV for both rutile and α -MnO₂ crystal structures (Figure 11b). Thus, these results clearly demonstrate that not only the 1D nanorod morphology benefits the improvement in the catalytic activity but also the crystal structure itself plays a major role in enhancing the catalytic activity (since our calculations did not involve any considerations of the different morphologies of nanostructured surfaces). Accordingly, the present theoretical results correspondingly attest to the excellent electrocatalytic performance of the as-synthesized α -(Mn,Ir)O₂ NRs for the OER in PEM water electrolysis. In addition, the current theoretical work also provides an excellent pathway to engineer high-performance nonprecious OER electrocatalysts for efficient hydrogen production via PEM-based acid mediated water electrolysis.

4. CONCLUSIONS

In summary, we have demonstrated a facile hydrothermal and wet chemical approach for the synthesis of 1D (Mn_{0.8}Ir_{0.2})O₂:10F nanorods (NRs) as an efficient electrocatalyst for the acidic OER. The as-synthesized (Mn_{0.8}Ir_{0.2})O₂:10F NRs possessing a unique electronic/molecular structure exhibit notable electrochemical activity with a lower onset

potential of ~ 1.35 V (vs RHE) in comparison to that of IrO₂ (~ 1.43 V vs RHE). In addition, owing to the presence of 1D channels in the nanorod architecture and unique electronic structure obtained upon formation of fluorine (F)-containing solid solutions, the (Mn_{0.8}Ir_{0.2})O₂:10F NRs exhibit low charge transfer resistance ($\sim 2.5 \Omega \text{ cm}^2$), low Tafel slope ($\sim 38 \text{ mV dec}^{-1}$), high electrochemically active surface area (ECSA $\approx 704.76 \text{ m}^2 \text{ g}^{-1}$), and notable OER performance with ~ 6 -, ~ 2.1 -, and ~ 2.2 -fold higher electrocatalytic activity in comparison to IrO₂, (Mn_{0.8}Ir_{0.2})O₂ NRs, and 2D thin film of (Mn_{0.8}Ir_{0.2})O₂:10F, respectively. Additionally, considerably higher ECSA and BET specific activity, mass activity (40 A g^{-1}), and TOF (0.01 s^{-1}) at an overpotential of ~ 220 mV clearly suggest the intrinsically higher electrocatalytic activity of (Mn_{0.8}Ir_{0.2})O₂:10F NRs in comparison to the other as-synthesized electrocatalysts. Moreover, in a 24 h OER durability study, no major deviation in current density was witnessed for our as-synthesized (Mn_{0.8}Ir_{0.2})O₂:10F NRs, suggesting its structural robustness and chemical as well as electrochemical integrity for displaying the sustained and prolonged OER response under harsh acidic conditions, which is also competently reinforced by the poststability characterization analyses. Furthermore, our extensive DFT calculations suggest that the solid solution of α -MnO₂-based crystal structure ((Mn_{0.8}Ir_{0.2})O₂:10F) demonstrates electrocatalytic activity higher than that of a rutile MnO₂ based crystal structure with the similar chemical composition and ionic distribution. Also, the results reported herein further demonstrate the inherent capability of MnO₂ to promote the OER reaction if it can be made to display high electronic conductivity combined with the required electrochemical stability for the OER in acidic media. Indeed, following the pathway discussed herein, doping with some non-noble materials could meet these requirements, transforming the electronic structure and thus opening new pathways for synthesizing novel families of platinum group metal (PGM) free electrocatalysts for PEM water electrolysis. Correspondingly, the present work demonstrates the fidelity of the 1D (Mn,Ir)O₂:10F nanorod electrocatalyst system for efficient hydrogen generation and water splitting via PEM-based acid mediated water electrolysis.

■ ASSOCIATED CONTENT

Supporting Information

The Supporting Information is available free of charge on the ACS Publications website at DOI: 10.1021/acscatal.8b02901.

Equations and calculation details, ECSA, roughness factor, mass activity, specific activity, TOF results, ICP-OES results, pore size distribution results, SEM elemental maps, EDX spectra, NMR data, Tafel slopes, EIS and LSV

results of MnO₂:10F, IrO₂:010F, and Nafion/Ti, poststability results of XRD, SEM, XPS, and LSV, and a comparison table of acidic OER electrocatalytic activity (PDF)

AUTHOR INFORMATION

Corresponding Author

*P.N.K.: e-mail, pkumta@pitt.edu; tel, +1-412-648-0223; fax, +1-412-624-3699.

ORCID

Prashant N. Kumta: 0000-0003-1227-1249

Author Contributions

The original concept of the present work was conceived by S.D.G. and P.N.K. S.D.G. designed the experiments, synthesized the electrocatalyst materials, performed physical–electrochemical characterizations, and analyzed the electrochemical data. O.I.V. conducted the theoretical analyses. S.D.G., S.T. (TEM), P.M.S. (XPS), and K.D. (NMR) performed and analyzed the structural and physical characterizations. M.K.D., O.I.V., P.M.S., S.T., K.D., and P.N.K. made important suggestions to the draft components. S.D.G. and O.I.V. wrote the first draft of the paper, and all authors participated in the manuscript development. The project was conceived and supervised by P.N.K.

Notes

The authors declare no competing financial interest.

ACKNOWLEDGMENTS

The authors acknowledge the financial support of the National Science Foundation, CBET-Grant 0933141 and CBET-Grant 1511390 for the present research. The authors are also grateful to the U.S. Department of Energy, Office of Basic Energy Sciences, Division of Materials Sciences and Engineering, under Award DE-SC0001531 for the support on our earlier work on OER electrocatalysts for PEM water electrolysis. The authors also gratefully acknowledge the Extreme Science and Engineering Discovery Environment (XSEDE)¹²⁵ supported by National Science Foundation grant number ACI-1053575, for providing the computational resources needed to complete the theoretical component of the present study. The authors acknowledge the Center for Complex Engineered Multifunctional Materials (CCEMM) as well as the Edward R. Weidlein Chair Professorship funds for offering the electrochemical equipment and facilities needed and utilized to complete the current research work.

REFERENCES

- (1) Obama, B. The Irreversible Momentum of Clean Energy. *Science* **2017**, *355*, 126–129.
- (2) Ghadge, S. D.; Patel, P. P.; Datta, M. K.; Velikokhatnyi, O. I.; Kuruba, R.; Shanthi, P. M.; Kumta, P. N. Fluorine Substituted (Mn,Ir)O₂:F High Performance Solid Solution Oxygen Evolution Reaction Electro-Catalysts for Pem Water Electrolysis. *RSC Adv.* **2017**, *7*, 17311–17324.
- (3) Ghadge, S. D.; Patel, P. P.; Datta, M. K.; Velikokhatnyi, O. I.; Shanthi, P. M.; Kumta, P. N. First Report of Vertically Aligned (Sn,Ir)O₂:F Solid Solution Nanotubes: Highly Efficient and Robust Oxygen Evolution Electrocatalysts for Proton Exchange Membrane Based Water Electrolysis. *J. Power Sources* **2018**, *392*, 139–149.
- (4) Dunn, S. Hydrogen Futures: Toward a Sustainable Energy System. *Int. J. Hydrogen Energy* **2002**, *27*, 235–264.
- (5) Patel, P. P.; Velikokhatnyi, O. I.; Ghadge, S. D.; Jampani, P. H.; Datta, M. K.; Hong, D.; Poston, J. A.; Manivannan, A.; Kumta, P. N. Highly Active Robust Oxide Solid Solution Electro-Catalysts for

Oxygen Reduction Reaction for Proton Exchange Membrane Fuel Cell and Direct Methanol Fuel Cell Cathodes. *Int. J. Hydrogen Energy* **2017**, *42*, 24079–24089.

(6) Patel, P. P.; Velikokhatnyi, O. I.; Ghadge, S. D.; Hanumantha, P. J.; Datta, M. K.; Kuruba, R.; Gattu, B.; Shanthi, P. M.; Kumta, P. N. Electrochemically Active and Robust Cobalt Doped Copper Phosphosulfide Electro-Catalysts for Hydrogen Evolution Reaction in Electrolytic and Photoelectrochemical Water Splitting. *Int. J. Hydrogen Energy* **2018**, *43*, 7855–7871.

(7) Azadi, G.; Bagheri, R.; Bikas, R.; Mousazade, Y.; Cui, J.; Song, Z.; Kinzhybalov, V.; Shen, J.-R.; Allakhverdiev, S. I.; Najafpour, M. M. A Transparent Electrode with Water-Oxidizing Activity. *Int. J. Hydrogen Energy* **2018**, *43*, 22896–22904.

(8) Carmo, M.; Fritz, D. L.; Mergel, J.; Stolten, D. A Comprehensive Review on Pem Water Electrolysis. *Int. J. Hydrogen Energy* **2013**, *38*, 4901–4934.

(9) Santos, D. M. F.; Sequeira, C. A. C.; Figueiredo, J. L. Hydrogen Production by Alkaline Water Electrolysis. *Quim. Nova* **2013**, *36*, 1176–1193.

(10) Marshall, A. T.; Sunde, S.; Tsympkin, M.; Tunold, R. Performance of a Pem Water Electrolysis Cell Using Irxruytazo₂ Electrocatalysts for the Oxygen Evolution Electrode. *Int. J. Hydrogen Energy* **2007**, *32*, 2320–2324.

(11) Badam, R.; Hara, M.; Huang, H.-H.; Yoshimura, M. Synthesis and Electrochemical Analysis of Novel IrO₂ Nanoparticle Catalysts Supported on Carbon Nanotube for Oxygen Evolution Reaction. *Int. J. Hydrogen Energy* **2018**, *43*, 18095–18104.

(12) Patel, P. P.; Ghadge, S. D.; Hanumantha, P. J.; Datta, M. K.; Gattu, B.; Shanthi, P. M.; Kumta, P. N. Active and Robust Novel Bilayer Photoanode Architectures for Hydrogen Generation Via Direct Non-Electric Bias Induced Photo-Electrochemical Water Splitting. *Int. J. Hydrogen Energy* **2018**, *43*, 13158–13176.

(13) Railsback, L. B. An Earth Scientist's Periodic Table of the Elements and Their Ions. *Geology* **2003**, *31*, 737–740.

(14) Grigoriev, S. A.; Porembsky, V. I.; Fateev, V. N. Pure Hydrogen Production by Pem Electrolysis for Hydrogen Energy. *Int. J. Hydrogen Energy* **2006**, *31*, 171–175.

(15) Tariq, M.; Zaman, W. Q.; Sun, W.; Zhou, Z.; Wu, Y.; Cao, L.-m.; Yang, J. Unraveling the Beneficial Electrochemistry of IrO₂/MoO₃ Hybrid as a Highly Stable and Efficient Oxygen Evolution Reaction Catalyst. *ACS Sustainable Chem. Eng.* **2018**, *6*, 4854–4862.

(16) Datta, M. K.; Kadakia, K.; Velikokhatnyi, O. I.; Jampani, P. H.; Chung, S. J.; Poston, J. A.; Manivannan, A.; Kumta, P. N. High Performance Robust F-Doped Tin Oxide Based Oxygen Evolution Electro-Catalysts for Pem Based Water Electrolysis. *J. Mater. Chem. A* **2013**, *1*, 4026–4037.

(17) Kadakia, K. S.; Jampani, P.; Velikokhatnyi, O. I.; Datta, M. K.; Chung, S. J.; Poston, J. A.; Manivannan, A.; Kumta, P. N. Nanostructured (Ir, Sn) O₂: F–Oxygen Evolution Reaction Anode Electro-Catalyst Powders for Pem Based Water Electrolysis. *J. Electrochem. Soc.* **2014**, *161*, F868–F875.

(18) Kadakia, K. S.; Jampani, P. H.; Velikokhatnyi, O. I.; Datta, M. K.; Park, S. K.; Hong, D. H.; Chung, S. J.; Kumta, P. N. Nanostructured F Doped IrO₂ Electro-Catalyst Powders for Pem Based Water Electrolysis. *J. Power Sources* **2014**, *269*, 855–865.

(19) Velikokhatnyi, O. I.; Kadakia, K.; Datta, M. K.; Kumta, P. N. Fluorine-Doped IrO₂: A Potential Electrocatalyst for Water Electrolysis. *J. Phys. Chem. C* **2013**, *117*, 20542–20547.

(20) Kadakia, K.; Datta, M. K.; Velikokhatnyi, O. I.; Jampani, P.; Park, S. K.; Saha, P.; Poston, J. A.; Manivannan, A.; Kumta, P. N. Novel (Ir, Sn, Nb) O₂ Anode Electrocatalysts with Reduced Noble Metal Content for Pem Based Water Electrolysis. *Int. J. Hydrogen Energy* **2012**, *37*, 3001–3013.

(21) Kadakia, K.; Datta, M. K.; Velikokhatnyi, O. I.; Jampani, P. H.; Kumta, P. N. Fluorine Doped (Ir, Sn, Nb) O₂ Anode Electro-Catalyst for Oxygen Evolution Via Pem Based Water Electrolysis. *Int. J. Hydrogen Energy* **2014**, *39*, 664–674.

- (22) Wu, H. B.; Zhang, G.; Yu, L.; Lou, X. W. D. One-Dimensional Metal Oxide–Carbon Hybrid Nanostructures for Electrochemical Energy Storage. *Nanoscale Horiz.* **2016**, *1*, 27–40.
- (23) Devan, R. S.; Patil, R. A.; Lin, J. H.; Ma, Y. R. One-Dimensional Metal-Oxide Nanostructures: Recent Developments in Synthesis, Characterization, and Applications. *Adv. Funct. Mater.* **2012**, *22*, 3326–3370.
- (24) Kim, Y.; Kim, J. G.; Noh, Y.; Kim, W. B. An Overview of One-Dimensional Metal Nanostructures for Electrocatalysis. *Catal. Surv. Asia* **2015**, *19*, 88–121.
- (25) Lu, Y.; Du, S.; Steinberger-Wilckens, R. One-Dimensional Nanostructured Electrocatalysts for Polymer Electrolyte Membrane Fuel Cells—a Review. *Appl. Catal., B* **2016**, *199*, 292–314.
- (26) Li, J.; Zheng, G. One-Dimensional Earth-Abundant Nanomaterials for Water-Splitting Electrocatalysts. *Advanced Science* **2017**, *4*, 1600380.
- (27) Zhu, Y. P.; Liu, Y. P.; Ren, T. Z.; Yuan, Z. Y. Self-Supported Cobalt Phosphide Mesoporous Nanorod Arrays: A Flexible and Bifunctional Electrode for Highly Active Electrocatalytic Water Reduction and Oxidation. *Adv. Funct. Mater.* **2015**, *25*, 7337–7347.
- (28) Feng, L.-L.; Yu, G.; Wu, Y.; Li, G.-D.; Li, H.; Sun, Y.; Asefa, T.; Chen, W.; Zou, X. High-Index Faceted Ni₃S₂ Nanosheet Arrays as Highly Active and Ultrastable Electrocatalysts for Water Splitting. *J. Am. Chem. Soc.* **2015**, *137*, 14023–14026.
- (29) Kundu, S.; Nagaiah, T. C.; Xia, W.; Wang, Y.; Dommele, S. V.; Bitter, J. H.; Santa, M.; Grundmeier, G.; Bron, M.; Schuhmann, W. Electrocatalytic Activity and Stability of Nitrogen-Containing Carbon Nanotubes in the Oxygen Reduction Reaction. *J. Phys. Chem. C* **2009**, *113*, 14302–14310.
- (30) Gong, K.; Du, F.; Xia, Z.; Durstock, M.; Dai, L. Nitrogen-Doped Carbon Nanotube Arrays with High Electrocatalytic Activity for Oxygen Reduction. *Science* **2009**, *323*, 760.
- (31) Cho, I. S.; Chen, Z.; Forman, A. J.; Kim, D. R.; Rao, P. M.; Jaramillo, T. F.; Zheng, X. Branched TiO₂ Nanorods for Photoelectrochemical Hydrogen Production. *Nano Lett.* **2011**, *11*, 4978–4984.
- (32) Liu, J.; Bai, H.; Wang, Y.; Liu, Z.; Zhang, X.; Sun, D. D. Self-Assembling TiO₂ Nanorods on Large Graphene Oxide Sheets at a Two-Phase Interface and Their Anti-Recombination in Photocatalytic Applications. *Adv. Funct. Mater.* **2010**, *20*, 4175–4181.
- (33) Wolcott, A.; Smith, W. A.; Kuykendall, T. R.; Zhao, Y.; Zhang, J. Z. Photoelectrochemical Water Splitting Using Dense and Aligned TiO₂ Nanorod Arrays. *Small* **2009**, *5*, 104–111.
- (34) He, H.; Xiao, P.; Zhou, M.; Liu, F.; Yu, S.; Qiao, L.; Zhang, Y. Pt_{ni} Alloy Nanoparticles Supported on Carbon-Doped TiO₂ Nanotube Arrays for Photo-Assisted Methanol Oxidation. *Electrochim. Acta* **2013**, *88*, 782–789.
- (35) Koenigsmann, C.; Wong, S. S. One-Dimensional Noble Metal Electrocatalysts: A Promising Structural Paradigm for Direct Methanol Fuel Cells. *Energy Environ. Sci.* **2011**, *4*, 1161–1176.
- (36) Jiang, Q.-Z.; Wu, X.; Shen, M.; Ma, Z.-F.; Zhu, X.-Y. Low-Pt Content Carbon-Supported Pt–Ni–TiO₂ Nanotube Electrocatalyst for Direct Methanol Fuel Cells. *Catal. Lett.* **2008**, *124*, 434–438.
- (37) Chen, P.; Xu, K.; Fang, Z.; Tong, Y.; Wu, J.; Lu, X.; Peng, X.; Ding, H.; Wu, C.; Xie, Y. Metallic Co_{4n} Porous Nanowire Arrays Activated by Surface Oxidation as Electrocatalysts for the Oxygen Evolution Reaction. *Angew. Chem.* **2015**, *127*, 14923–14927.
- (38) Alia, S. M.; Shulda, S.; Ngo, C.; Pylypenko, S.; Pivovar, B. S. Iridium-Based Nanowires as Highly Active, Oxygen Evolution Reaction Electrocatalysts. *ACS Catal.* **2018**, *8*, 2111–2120.
- (39) Wang, H.; Lu, Z.; Qian, D.; Li, Y.; Zhang, W. Single-Crystal A-MnO₂ Nanorods: Synthesis and Electrochemical Properties. *Nanotechnology* **2007**, *18*, 115616.
- (40) Zhao, C.; Yu, H.; Li, Y.; Li, X.; Ding, L.; Fan, L. Electrochemical Controlled Synthesis and Characterization of Well-Aligned IrO₂ Nanotube Arrays with Enhanced Electrocatalytic Activity toward Oxygen Evolution Reaction. *J. Electroanal. Chem.* **2013**, *688*, 269–274.
- (41) Liu, H.; Song, C.; Zhang, L.; Zhang, J.; Wang, H.; Wilkinson, D. P. A Review of Anode Catalysis in the Direct Methanol Fuel Cell. *J. Power Sources* **2006**, *155*, 95–110.
- (42) Chen, Z.; Waje, M.; Li, W.; Yan, Y. Supportless Pt and PtPd Nanotubes as Electrocatalysts for Oxygen-Reduction Reactions. *Angew. Chem., Int. Ed.* **2007**, *46*, 4060–4063.
- (43) Garbarino, S.; Ponrouch, A.; Pronovost, S.; Gaudet, J.; Guay, D. Synthesis and Characterization of Preferentially Oriented (1 0 0) Pt Nanowires. *Electrochem. Commun.* **2009**, *11*, 1924–1927.
- (44) Xiang, B.; Wang, P.; Zhang, X.; Dayeh, S. A.; Aplin, D. P. R.; Soci, C.; Yu, D.; Wang, D. Rational Synthesis of P-Type Zinc Oxide Nanowire Arrays Using Simple Chemical Vapor Deposition. *Nano Lett.* **2007**, *7*, 323–328.
- (45) Puentes, V. F.; Krishnan, K. M.; Alivisatos, A. P. Colloidal Nanocrystal Shape and Size Control: The Case of Cobalt. *Science* **2001**, *291*, 2115–2117.
- (46) Li, S. Y.; Lin, P.; Lee, C. Y.; Tseng, T. Y. Field Emission and Photofluorescent Characteristics of Zinc Oxide Nanowires Synthesized by a Metal Catalyzed Vapor-Liquid-Solid Process. *J. Appl. Phys.* **2004**, *95*, 3711–3716.
- (47) Sun, W.; Cao, L.-m.; Yang, J. Conversion of Inert Cryptomelane-Type Manganese Oxide into a Highly Efficient Oxygen Evolution Catalyst Via Limited Ir Doping. *J. Mater. Chem. A* **2016**, *4*, 12561–12570.
- (48) Cheng, F.; Zhao, J.; Song, W.; Li, C.; Ma, H.; Chen, J.; Shen, P. Facile Controlled Synthesis of MnO₂ Nanostructures of Novel Shapes and Their Application in Batteries. *Inorg. Chem.* **2006**, *45*, 2038–2044.
- (49) Yuan, Z.-Y.; Ren, T.-Z.; Du, G.; Su, B.-L. A Facile Preparation of Single-Crystalline α -Mn₂O₃ Nanorods by Ammonia-Hydrothermal Treatment of MnO₂. *Chem. Phys. Lett.* **2004**, *389*, 83–86.
- (50) Ye, Z.-G.; Meng, H.-M.; Chen, D.; Yu, H.-Y.; Huan, Z.-S.; Wang, X.-D.; Sun, D.-B. Structure and Characteristics of Ti/IrO₂(X)+MnO₂(1–X) Anode for Oxygen Evolution. *Solid State Sci.* **2008**, *10*, 346–354.
- (51) Geiger, S.; Kasian, O.; Shrestha, B. R.; Mingers, A. M.; Mayrhofer, K. J. J.; Cherevko, S. Activity and Stability of Electrochemically and Thermally Treated Iridium for the Oxygen Evolution Reaction. *J. Electrochem. Soc.* **2016**, *163*, F3132–F3138.
- (52) Siracusano, S.; Baglio, V.; Grigoriev, S. A.; Merlo, L.; Fateev, V. N.; Aricò, A. S. The Influence of Iridium Chemical Oxidation State on the Performance and Durability of Oxygen Evolution Catalysts in Pem Electrolysis. *J. Power Sources* **2017**, *366*, 105–114.
- (53) Rossmel, J.; Qu, Z. W.; Zhu, H.; Kroes, G. J.; Nørskov, J. K. Electrolysis of Water on Oxide Surfaces. *J. Electroanal. Chem.* **2007**, *607*, 83–89.
- (54) Bligaard, T.; Nørskov, J. K. Ligand Effects in Heterogeneous Catalysis and Electrochemistry. *Electrochim. Acta* **2007**, *52*, 5512–5516.
- (55) Kresse, G.; Furthmüller, J. Efficiency of Ab-Initio Total Energy Calculations for Metals and Semiconductors Using a Plane-Wave Basis Set. *Comput. Mater. Sci.* **1996**, *6*, 15–50.
- (56) Perdew, J. P.; Burke, K.; Ernzerhof, M. Generalized Gradient Approximation Made Simple. *Phys. Rev. Lett.* **1996**, *77*, 3865–3868.
- (57) Kresse, G.; Joubert, D. From Ultrasoft Pseudopotentials to the Projector Augmented-Wave Method. *Phys. Rev. B: Condens. Matter Phys.* **1999**, *59*, 1758–1775.
- (58) Chen, R.-S.; Huang, Y.-S.; Liang, Y.-M.; Tsai, D.-S.; Chi, Y.; Kai, J.-J. Growth Control and Characterization of Vertically Aligned IrO₂ Nanorods. *J. Mater. Chem.* **2003**, *13*, 2525–2529.
- (59) Kavar, R. K.; Chigare, P. S.; Patil, P. S. Substrate Temperature Dependent Structural, Optical and Electrical Properties of Spray Deposited Iridium Oxide Thin Films. *Appl. Surf. Sci.* **2003**, *206*, 90–101.
- (60) Shilpa, N.; Manna, J.; Rajput, P.; Rana, R. K. Water Oxidation Catalyst Via Heterogenization of Iridium Oxides on Silica: A Polyamine-Mediated Route to Achieve Activity and Stability. *ACS Catal.* **2016**, *6*, 5699–5705.

- (61) Deshmukh, A. V.; Patil, S. I.; Yusuf, S. M.; Rajarajan, A. K.; Lalla, N. P. Structural, Chemical and Magnetic Investigations of Polycrystalline Zn_{1-x}Mn_xO. *J. Magn. Magn. Mater.* **2010**, *322*, 536–541.
- (62) Chung, H.-T.; Kim, J.-G.; Kim, H.-G. Dependence of the Lithium Ionic Conductivity on the B-Site Ion Substitution in (Li_{0.5}La_{0.5})Ti_{1-x}MxO₃ (M= Sn, Zr, Mn, Ge). *Solid State Ionics* **1998**, *107*, 153–160.
- (63) Choy, J.-H.; Kim, D.-K.; Hwang, S.-H.; Demazeau, G.; Jung, D.-Y. Xanes and EXAFS Studies on the Ir-O Bond Covalency in Ionic Iridium Perovskites. *J. Am. Chem. Soc.* **1995**, *117*, 8557–8566.
- (64) Wu, Y.; Li, S.; Cao, Y.; Xing, S.; Ma, Z.; Gao, Y. Facile Synthesis of Mesoporous A-MnO₂ Nanorod with Three-Dimensional Frameworks and Its Enhanced Catalytic Activity for Voc's Removal. *Mater. Lett.* **2013**, *97*, 1–3.
- (65) Yuan, W.; Wang, B.; Wu, H.; Xiang, M.; Wang, Q.; Liu, H.; Zhang, Y.; Liu, H.; Dou, S. A Flexible 3d Nitrogen-Doped Carbon Foam@Cnts Hybrid Hosting TiO₂ Nanoparticles as Free-Standing Electrode for Ultra-Long Cycling Lithium-Ion Batteries. *J. Power Sources* **2018**, *379*, 10–19.
- (66) Li, L.; Nan, C.; Lu, J.; Peng, Q.; Li, Y. A-MnO₂ Nanotubes: High Surface Area and Enhanced Lithium Battery Properties. *Chem. Commun.* **2012**, *48*, 6945–6947.
- (67) Liang, X.; Hart, C.; Pang, Q.; Garsuch, A.; Weiss, T.; Nazar, L. F. A Highly Efficient Polysulfide Mediator for Lithium–Sulfur Batteries. *Nat. Commun.* **2015**, *6*, 5682.
- (68) Nesbitt, H. W.; Banerjee, D. Interpretation of Xps Mn (2p) Spectra of Mn Oxyhydroxides and Constraints on the Mechanism of MnO₂ Precipitation. *Am. Mineral.* **1998**, *83*, 305–315.
- (69) Pfeifer, V.; Jones, T. E.; Vélez, J. J. V.; Massué, C.; Greiner, M. T.; Arrigo, R.; Teschner, D.; Girgsdies, F.; Scherzer, M.; Allan, J.; Hashagen, M.; Weinberg, G.; Piccinin, S.; Hävecker, M.; Knop-Gericke, A.; Schlögl, R. The Electronic Structure of Iridium Oxide Electrodes Active in Water Splitting. *Phys. Chem. Chem. Phys.* **2016**, *18*, 2292–2296.
- (70) Pfeifer, V.; Jones, T. E.; Velasco Vélez, J. J.; Massué, C.; Arrigo, R.; Teschner, D.; Girgsdies, F.; Scherzer, M.; Greiner, M. T.; Allan, J.; Hashagen, M.; Weinberg, G.; Piccinin, S.; Hävecker, M.; Knop-Gericke, A.; Schlögl, R. The Electronic Structure of Iridium and Its Oxides. *Surf. Interface Anal.* **2016**, *48*, 261–273.
- (71) Freakley, S. J.; Ruiz-Esquius, J.; Morgan, D. J. The X-Ray Photoelectron Spectra of Ir, IrO₂ and IrCl₃ Revisited. *Surf. Interface Anal.* **2017**, *49*, 794–799.
- (72) Lu, Z.-X.; Shi, Y.; Yan, C.-F.; Guo, C.-Q.; Wang, Z.-D. Investigation on IrO₂ Supported on Hydrogenated TiO₂ Nanotube Array as OER Electro-Catalyst for Water Electrolysis. *Int. J. Hydrogen Energy* **2017**, *42*, 3572–3578.
- (73) Wertheim, G. K.; Guggenheim, H. J. Conduction-Electron Screening in Metallic Oxides: IrO₂. *Phys. Rev. B: Condens. Matter Mater. Phys.* **1980**, *22*, 4680.
- (74) Oh, H.-S.; Nong, H. N.; Reier, T.; Bergmann, A.; Gliech, M.; Ferreira de Araujo, J.; Willinger, E.; Schlögl, R.; Teschner, D.; Strasser, P. Electrochemical Catalyst–Support Effects and Their Stabilizing Role for IrO_x Nanoparticle Catalysts During the Oxygen Evolution Reaction. *J. Am. Chem. Soc.* **2016**, *138*, 12552–12563.
- (75) Nong, H. N.; Gan, L.; Willinger, E.; Teschner, D.; Strasser, P. Irox Core-Shell Nanocatalysts for Cost- and Energy-Efficient Electrochemical Water Splitting. *Chemical Science* **2014**, *5*, 2955–2963.
- (76) Zhang, G.; Han, X.; Bian, W.; Zhan, J.; Ma, X. Facile Synthesis and High Formaldehyde-Sensing Performance of NiO–SnO₂ Hybrid Nanospheres. *RSC Adv.* **2016**, *6*, 3919–3926.
- (77) Ishfaq, M.; Rizwan Khan, M.; Bhopal, M. F.; Nasim, F.; Ali, A.; Bhatti, A. S.; Ahmed, I.; Bhardwaj, S.; Cepek, C. 1.5 MeV Proton Irradiation Effects on Electrical and Structural Properties of TiO₂/N-Si Interface. *J. Appl. Phys.* **2014**, *115*, 174506.
- (78) Sheng, Y.; Botero, M. L.; Manuputty, M. Y.; Kraft, M.; Xu, R. Co₃O₄ and Fe_xCo_{3-x}O₄ Nanoparticles/Films Synthesized in a Vapor-Fed Flame Aerosol Reactor for Oxygen Evolution. *ACS Appl. Energy Mater.* **2018**, *1*, 655–665.
- (79) Shaltout, A. A.; Afify, H. H.; Ali, S. A. Elucidation of Fluorine in SnO₂: F Sprayed Films by Different Spectroscopic Techniques. *J. Electron Spectrosc. Relat. Phenom.* **2012**, *185*, 140–145.
- (80) Amanullah, F. M.; Pratap, K. J.; Babu, V. H. Compositional Analysis and Depth Profile Studies on Undoped and Doped Tin Oxide Films Prepared by Spray Technique. *Mater. Sci. Eng., B* **1998**, *52*, 93–98.
- (81) Fantini, M.; Torriani, I. The Compositional and Structural Properties of Sprayed SnO₂: F Thin Films. *Thin Solid Films* **1986**, *138*, 255–265.
- (82) Sun, X.; Zhang, Y.; Song, P.; Pan, J.; Zhuang, L.; Xu, W.; Xing, W. Fluorine-Doped Carbon Blacks: Highly Efficient Metal-Free Electrocatalysts for Oxygen Reduction Reaction. *ACS Catal.* **2013**, *3*, 1726–1729.
- (83) Borrás, A.; Lopez, C.; Rico, V.; Gracia, F.; Gonzalez-Elipse, A. R.; Richter, E.; Battiston, G.; Gerbasí, R.; McSparran, N.; Sauthier, G. Effect of Visible and UV Illumination on the Water Contact Angle of TiO₂ Thin Films with Incorporated Nitrogen. *J. Phys. Chem. C* **2007**, *111*, 1801–1808.
- (84) Dubal, D. P.; Kim, W. B.; Lokhande, C. D. Galvanostatically Deposited Fe: MnO₂ Electrodes for Supercapacitor Application. *J. Phys. Chem. Solids* **2012**, *73*, 18–24.
- (85) Hu, Y.; Zhu, H.; Wang, J.; Chen, Z. Synthesis of Layered Birnessite-Type Manganese Oxide Thin Films on Plastic Substrates by Chemical Bath Deposition for Flexible Transparent Supercapacitors. *J. Alloys Compd.* **2011**, *509*, 10234–10240.
- (86) Li, R.; Liu, L.; Zhang, Y.; Yang, F. Preparation of a Nano-MnO₂ Surface-Modified Reduced Graphene Oxide/Pvdf Flat Sheet Membrane for Adsorptive Removal of Aqueous Ni (II). *RSC Adv.* **2016**, *6*, 20542–20550.
- (87) Moilanen, D. E.; Piletic, I. R.; Fayer, M. D. Water Dynamics in Nafion Fuel Cell Membranes: The Effects of Confinement and Structural Changes on the Hydrogen Bond Network. *J. Phys. Chem. C* **2007**, *111*, 8884–8891.
- (88) Korzeniewski, C.; Adams, E.; Liu, D. Responses of Hydrophobic and Hydrophilic Groups in Nafion Differentiated by Least Squares Modeling of Infrared Spectra Recorded During Thin Film Hydration. *Appl. Spectrosc.* **2008**, *62*, 634–639.
- (89) Vol'fkovich, Y. M.; Sosnenkin, V. E.; Nikol'skaya, N. F. Hydrophilic-Hydrophobic and Sorption Properties of the Catalyst Layers of Electrodes in a Proton-Exchange Membrane Fuel Cell: A Stage-by-Stage Study. *Russ. J. Electrochem.* **2010**, *46*, 438–449.
- (90) Sivanantham, A.; Ganesan, P.; Shanmugam, S. Hierarchical NiCo₂S₄ Nanowire Arrays Supported on Ni Foam: An Efficient and Durable Bifunctional Electrocatalyst for Oxygen and Hydrogen Evolution Reactions. *Adv. Funct. Mater.* **2016**, *26*, 4661–4672.
- (91) Cheng, F.; Su, Y.; Liang, J.; Tao, Z.; Chen, J. MnO₂-Based Nanostructures as Catalysts for Electrochemical Oxygen Reduction in Alkaline Media. *Chem. Mater.* **2010**, *22*, 898–905.
- (92) Mohammad, A. M.; Awad, M. I.; El-Deab, M. S.; Okajima, T.; Ohsaka, T. Electrocatalysis by Nanoparticles: Optimization of the Loading Level and Operating Ph for the Oxygen Evolution at Crystallographically Oriented Manganese Oxide Nanorods Modified Electrodes. *Electrochim. Acta* **2008**, *53*, 4351–4358.
- (93) Morita, M.; Iwakura, C.; Tamura, H. The Anodic Characteristics of Manganese Dioxide Electrodes Prepared by Thermal Decomposition of Manganese Nitrate. *Electrochim. Acta* **1977**, *22*, 325–328.
- (94) Reier, T.; Oezaslan, M.; Strasser, P. Electrocatalytic Oxygen Evolution Reaction (OER) on Ru, Ir, and Pt Catalysts: A Comparative Study of Nanoparticles and Bulk Materials. *ACS Catal.* **2012**, *2*, 1765–1772.
- (95) Kötter, R.; Stucki, S. Stabilization of RuO₂ by IrO₂ for Anodic Oxygen Evolution in Acid Media. *Electrochim. Acta* **1986**, *31*, 1311–1316.
- (96) Abbott, D. F.; Lebedev, D.; Waltar, K.; Povia, M.; Nachttegaal, M.; Fabbri, E.; Coperet, C.; Schmidt, T. J. Iridium Oxide for the Oxygen Evolution Reaction: Correlation between Particle Size, Morphology, and the Surface Hydroxyl Layer from Operando XAS. *Chem. Mater.* **2016**, *28*, 6591–6604.

- (97) Binninger, T.; Mohamed, R.; Waltar, K.; Fabbri, E.; Levecque, P.; Kötzt, R.; Schmidt, T. J. Thermodynamic Explanation of the Universal Correlation between Oxygen Evolution Activity and Corrosion of Oxide Catalysts. *Sci. Rep.* **2015**, *5*, 12167.
- (98) Liang, H.; Meng, F.; Caban-Acevedo, M.; Li, L.; Forticaux, A.; Xiu, L.; Wang, Z.; Jin, S. Hydrothermal Continuous Flow Synthesis and Exfoliation of Nico Layered Double Hydroxide Nanosheets for Enhanced Oxygen Evolution Catalysis. *Nano Lett.* **2015**, *15*, 1421–1427.
- (99) Tong, Y.; Xu, J.; Jiang, H.; Gao, F.; Lu, Q. Thickness-Control of Ultrathin Two-Dimensional Cobalt Hydroxide Nanosheets with Enhanced Oxygen Evolution Reaction Performance. *Chem. Eng. J.* **2017**, *316*, 225–231.
- (100) Yan, K.-L.; Chi, J.-Q.; Xie, J.-Y.; Dong, B.; Liu, Z.-Z.; Gao, W.-K.; Lin, J.-H.; Chai, Y.-M.; Liu, C.-G. Mesoporous Ag-Doped Co₃O₄ Nanowire Arrays Supported on Fto as Efficient Electrocatalysts for Oxygen Evolution Reaction in Acidic Media. *Renewable Energy* **2018**, *119*, 54–61.
- (101) Abreu-Sepulveda, M.; Trinh, P.; Malkhandi, S.; Narayanan, S. R.; Jorné, J.; Quesnel, D. J.; Postonr, J. A.; Manivannan, A. Investigation of Oxygen Evolution Reaction at Laruo 3, La 3.5 Ru 4 O 13, and La 2 Ruo 5. *Electrochim. Acta* **2015**, *180*, 401–408.
- (102) Tackett, B. M.; Sheng, W.; Kattel, S.; Yao, S.; Yan, B.; Kuttiyiel, K. A.; Wu, Q.; Chen, J. G. Reducing Iridium Loading in Oxygen Evolution Reaction Electrocatalysts Using Core–Shell Particles with Nitride Cores. *ACS Catal.* **2018**, *8*, 2615–2621.
- (103) McCrory, C. C. L.; Jung, S.; Peters, J. C.; Jaramillo, T. F. Benchmarking Heterogeneous Electrocatalysts for the Oxygen Evolution Reaction. *J. Am. Chem. Soc.* **2013**, *135*, 16977–16987.
- (104) Mondschein, J. S.; Kumar, K.; Holder, C. F.; Seth, K.; Kim, H.; Schaak, R. E. Intermetallic Ni₂ta Electrocatalyst for the Oxygen Evolution Reaction in Highly Acidic Electrolytes. *Inorg. Chem.* **2018**, *57*, 6010–6015.
- (105) Wang, H.; Xu, C.; Cheng, F.; Zhang, M.; Wang, S.; Jiang, S. P. Pd/Pt Core–Shell Nanowire Arrays as Highly Effective Electrocatalysts for Methanol Electrooxidation in Direct Methanol Fuel Cells. *Electrochem. Commun.* **2008**, *10*, 1575–1578.
- (106) Tiwari, J. N.; Tiwari, R. N.; Kim, K. S. Zero-Dimensional, One-Dimensional, Two-Dimensional and Three-Dimensional Nanostructured Materials for Advanced Electrochemical Energy Devices. *Prog. Mater. Sci.* **2012**, *57*, 724–803.
- (107) Takashima, T.; Hashimoto, K.; Nakamura, R. Mechanisms of Ph-Dependent Activity for Water Oxidation to Molecular Oxygen by Mno₂ Electrocatalysts. *J. Am. Chem. Soc.* **2012**, *134*, 1519–1527.
- (108) Wang, M.; Jiang, J.; Ai, L. Layered Bimetallic Iron–Nickel Alkoxide Microspheres as High-Performance Electrocatalysts for Oxygen Evolution Reaction in Alkaline Media. *ACS Sustainable Chem. Eng.* **2018**, *6*, 6117–6125.
- (109) Takashima, T.; Hashimoto, K.; Nakamura, R. Inhibition of Charge Disproportionation of Mno₂ Electrocatalysts for Efficient Water Oxidation under Neutral Conditions. *J. Am. Chem. Soc.* **2012**, *134*, 18153–18156.
- (110) Huang, F.; Wan, Z.; Jin, Y.; Wen, L. The Effects of Cyclic Isothermal Oxidation on Ir/Irox Ph Electrode and a Method to Correct the Potential Drift of Metal Oxide Electrode. *J. Electrochem. Soc.* **2017**, *164*, B632–B640.
- (111) Dong, X.; Xu, Y.; Yan, S.; Mao, S.; Xiong, L.; Sun, X. Towards Low-Cost, High Energy Density Li₂ Mno₃ Cathode Materials. *J. Mater. Chem. A* **2015**, *3*, 670–679.
- (112) Kwon, T.; Hwang, H.; Sa, Y. J.; Park, J.; Baik, H.; Joo, S. H.; Lee, K. Cobalt Assisted Synthesis of Ircu Hollow Octahedral Nanocages as Highly Active Electrocatalysts toward Oxygen Evolution Reaction. *Adv. Funct. Mater.* **2017**, *27*, 1604688.
- (113) Lim, J.; Yang, S.; Kim, C.; Roh, C.-W.; Kwon, Y.; Kim, Y.-T.; Lee, H. Shaped Ir–Ni Bimetallic Nanoparticles for Minimizing Ir Utilization in Oxygen Evolution Reaction. *Chem. Commun.* **2016**, *52*, 5641–5644.
- (114) Lettenmeier, P.; Wang, L.; Golla-Schindler, U.; Gazdzicki, P.; Cañas, N. A.; Handl, M.; Hiesgen, R.; Hosseiny, S. S.; Gago, A. S.; Friedrich, K. A. Nanosized Irox–Ir Catalyst with Relevant Activity for Anodes of Proton Exchange Membrane Electrolysis Produced by a Cost-Effective Procedure. *Angew. Chem.* **2016**, *128*, 752–756.
- (115) Fu, Y.; Yu, H. Y.; Jiang, C.; Zhang, T. H.; Zhan, R.; Li, X.; Li, J. F.; Tian, J. H.; Yang, R. Nico Alloy Nanoparticles Decorated on N-Doped Carbon Nanofibers as Highly Active and Durable Oxygen Electrocatalyst. *Adv. Funct. Mater.* **2018**, *28*, 1705094.
- (116) Hammer, B.; Nørskov, J. K. Theoretical Surface Science and Catalysis—Calculations and Concepts. *Adv. Catal.* **2000**, *45*, 71–129.
- (117) Tripkovic, V.; Hansen, H. A.; Vegge, T. Computational Screening of Doped A-Mno₂ Catalysts for the Oxygen Evolution Reaction. *ChemSusChem* **2018**, *11*, 629–637.
- (118) Li, T.; Wu, J.; Xiao, X.; Zhang, B.; Hu, Z.; Zhou, J.; Yang, P.; Chen, X.; Wang, B.; Huang, L. Band Gap Engineering of Mno₂ through in Situ Al-Doping for Applicable Pseudocapacitors. *RSC Adv.* **2016**, *6*, 13914–13919.
- (119) Xu, C.; Kang, F.; Li, B.; Du, H. Recent Progress on Manganese Dioxide Based Supercapacitors. *J. Mater. Res.* **2010**, *25*, 1421–1432.
- (120) Frydendal, R.; Paoli, E. A.; Chorkendorff, I.; Rossmeisl, J.; Stephens, I. E. L. Toward an Active and Stable Catalyst for Oxygen Evolution in Acidic Media: Ti-Stabilized Mno₂. *Adv. Energy Mater.* **2015**, *5*, 1500991.
- (121) Shinde, A.; Jones, R. J. R.; Guevarra, D.; Mitrovic, S.; Becerra-Stasiewicz, N.; Haber, J. A.; Jin, J.; Gregoire, J. M. High-Throughput Screening for Acid-Stable Oxygen Evolution Electrocatalysts in the (Mn–Co–Ta–Sb) O X Composition Space. *Electrocatalysis* **2015**, *6*, 229–236.
- (122) Moreno-Hernandez, I. A.; MacFarland, C. A.; Read, C. G.; Papadantonakis, K. M.; Brunschwigg, B. S.; Lewis, N. S. Crystalline Nickel Manganese Antimonate as a Stable Water-Oxidation Catalyst in Aqueous 1.0 Mh₂So₄. *Energy Environ. Sci.* **2017**, *10*, 2103–2108.
- (123) Huynh, M.; Ozel, T.; Liu, C.; Lau, E. C.; Nocera, D. G. Design of Template-Stabilized Active and Earth-Abundant Oxygen Evolution Catalysts in Acid. *Chemical science* **2017**, *8*, 4779–4794.
- (124) Huynh, M.; Bediako, D. K.; Nocera, D. G. A Functionally Stable Manganese Oxide Oxygen Evolution Catalyst in Acid. *J. Am. Chem. Soc.* **2014**, *136*, 6002–6010.
- (125) Towns, J.; Cockerill, T.; Dahan, M.; Foster, I.; Gaither, K.; Grimshaw, A.; Hazlewood, V.; Lathrop, S.; Lifka, D.; Peterson, G. D.; Roskies, R.; Scott, J. R.; Wilkens-Diehr, N. XSEDE: Accelerating Scientific Discovery. *Comput. Sci. Eng.* **2014**, *16* (5), 62–74.